


國立交通大學

光電工程研究所

碩士論文

利用緊束縛理論研究光子晶體波導之耦合
行為與多工分波器設計



Tight-Binding Theory for Coupling of Identical Photonic
Crystal Waveguides and its application for
Wavelength-Division Multiplexing design

研究生：涂家斌

指導教授：謝文峰 教授

中華民國九十四年六月

Tight-Binding Theory for Coupling of Identical
Photonic Crystal Waveguides and its application for
Wavelength-Division Multiplexing design

Student: Jia-Bin Tu

Advisor: Prof. Wen-Feng Hsieh

A Thesis

Submitted to Institute of Electro-Optical Engineering
College of Electrical Engineering and Computer Science

National Chiao Tung University

in Partial Fulfillment of the Requirements

for the Degree of

Master of Engineering

in

Electro-Optical Engineering

June 2005

Hsinchu, Taiwan, Republic of China

利用緊束縛理論研究光子晶體波導之耦合 行為與多工分波器之設計

研究生：涂家斌

指導老師：謝文峰 教授

國立交通大學光電工程研究所

摘要

利用固態物理中的能帶緊束縛(Tight-binding)理論，可以正確地描述一個光子晶體波導的傳輸行為。利用此理論得到的光子晶體波導的色散關係方程式，可以進一步去描述兩條耦合光子晶體波導的傳輸行為和色散關係方程，並正確地計算其耦合長度(coupling length)，進而用以設計光通訊元件。

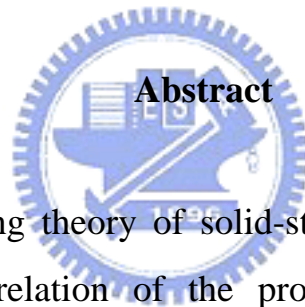
當兩個相同的光子晶體波導彼此靠得很近時，其能帶便會由於波導之間的耦合效應，而分裂為偶對稱與奇對稱的本徵模。由於耦合光子晶體波導與普通耦合光波導不同，除了橫向之耦合效應外，並具有縱向(傳播方向)之耦合，導致此兩種模態會發生能帶交叉的現象。因此，我們可以利用緊束縛理論所推導出來的色散關係方程式找到正確非耦合頻率(decoupled frequency)。利用此耦合波導的特殊特性，我們用“時域有限差分法(FDTD)”之數值模擬，完成了多工分波器(WDM)元件的設計。本論文中，我們可以將三道不同波長的光分開，且均達到光通訊的標準。

Tight-Binding Theory for Coupling of Identical Photonic Crystal Waveguides and its application for Wavelength-Division Multiplexing design

Student: Jia-Bin Tu

Advisor: Prof. Wen-Feng Hsieh

Institute of Electro-Optical Engineering
College of Electrical Engineering and Computer Science
National Chiao Tung University



By using tight-binding theory of solid-state physics, we can analytically describe the dispersion relation of the propagation in a photonic crystal waveguide (PCW). In turn, we can derive the dispersion curves of two coupled identical PCWs .

Due to not only the transverse coupling as the conventional coupled waveguides but also the longitudinal coupling of two coupled identical PCWs. “Band-crossing” may occur at which the PCWs will not couple with each other (or decoupled) when the coupled PCWs are placed close enough to each other. By employing the tight-binding theory to this problem, we can accurately determine the decoupling frequency as well as calculate the coupling length for every frequency. We have designed a wavelength division multiplexer which can route three wavelengths into different channels with the power ratio of all outputs reach 20 dB, the specification of optical communication.

誌 謝

天啊！歷經各種訓練、磨練、鍛鍊後，終於寫到這一章了，心中的激動已是筆墨難形地爽。兩年前還是一個懵懂無知的我，踏進交大，對於這邊的環境一點都不熟悉，心中充滿了忐忑不安，壓根沒想到畢業這兩個字，只能走一步算一步，後來來到了小天王實驗室，幸蒙各位學長青睞，得以進入這個氣氛超好的實驗室，讓我在這兩年的時光裡收穫很多，其中謝文峰老師當然是居功厥偉，因為老師個性好、平易近人、學識又超淵博，所以再笨的問題都敢發問，解決了我很多研究上甚至生活上的問題，真的十分感謝您；另外在研究上也很感謝程思誠老師、簡世森學長、黃志賢學長、和許育儒學長幫助我很多，我才能順利完成我的論文；還有實驗室的學長姐和我的一群好同學，有了你們，我的生活增添了許多歡樂，其中從北科來的那兩顆大頭，不好意思一直虧你們頭大，不過你們唱歌的功力以及學術上我是深深佩服的；阿笑都是你愛笑啦，害我也跟著瘋瘋癲癲，不過這樣也過的滿快樂的；還有阿勛跟小豪感謝你們也幫了我很多生活上的忙，博士班好好加油阿；還有我家人支持也是我能完成碩士生涯的原動力；最後當然還要感謝一個重要的人，那就是我的女朋友小嵐，謝謝妳一直陪在我身邊支持我鼓勵我，讓我能度過重重難關，以後也要一起加油唷！

Content

| | |
|--|-----------|
| Abstract (in Chinese)..... | i |
| Abstract (in English)..... | ii |
| Acknowledgements..... | iii |
| Content..... | iv |
| List of Tables..... | vi |
| List of Figures..... | vii |
| Chapter 1 Introduction..... | 1 |
| 1-1 Background..... | 1 |
| 1-2 Motivation..... | 4 |
| 1-3 Organization of the thesis..... | 5 |
| Chapter 2 Calculation Method and Theory..... | 6 |
| 2-1 Introduction..... | 6 |
| 2-2 Plane-wave expansion method..... | 8 |
| 2-3 Finite-difference time-domain method..... | 10 |
| 2-3.1 FDTD method in One-dimensional case..... | 11 |
| 2-3.2 Two-dimensional formulation and perfectly matched layer (PML) boundary condition..... | 15 |
| 2-4 Tight binding method in solid state physics..... | 18 |
| Chapter 3 Simulation and Discussion..... | 21 |
| 3-1 Long-range interaction of defect modes between coupled identical photonic | |

| | |
|---|-----------|
| crystal waveguides..... | 21 |
| 3-1.1 Single line defect photonic crystal waveguides and tight-binding approximation..... | 21 |
| 3-1.2 Tight-binding theory of coupling of identical photonic crystal waveguides | 28 |
| 3-1.3 Summary..... | 33 |
| 3-2 Photonic crystal WDM design for application of coupling..... | 34 |
| 3-2.1 Coupling of PCWs..... | 34 |
| 3-2.2 Coupling ring device between PCWs..... | 39 |
| 3-2.3 Photonic crystal WDM design and FDTD simulation..... | 41 |
| 3-2.4 Summary..... | 47 |
| Chapter 4 Conclusion and Perspectives..... | 48 |
| References..... | 49 |



List of Tables

| | | |
|-----------|--|----|
| Table 3-1 | The parameters of Fitting curve function of a single PCW | 25 |
| Table 3-2 | The parameters of Fitting curve functions of two single PCW..... | 32 |
| Table 3-3 | Output power ratios of WDM..... | 45 |



List of Figures

| | | |
|----------|--|----|
| Fig. 1-1 | (a) splitter (b) waveguide..... | 2 |
| Fig. 1-2 | Photonic-crystal micro-cavity laser..... | 2 |
| Fig. 1-3 | Distribution of the real part of electric field in a 90° bend of the dielectric rods PCs..... | 3 |
| Fig. 2-1 | Interleaving of the E and H fields in space and time in the FDTD formulation..... | 11 |
| Fig. 2-2 | Interleaving of the E and H fields for the 2-D TM formulation.... | 16 |
| Fig. 2-3 | Total field/scattered field of the 2-D problem space..... | 18 |
| Fig. 3-1 | (a) A single point defect (b) A diagram of coupled cavity waveguide (CCW)..... | 23 |
| Fig. 3-2 | Schematics of propagation of photons by the coupled evanescent defect modes..... | 23 |
| Fig. 3-3 | The defect at site n coupling with the l th neighboring defects..... | 24 |
| Fig. 3-4 | (a) (b) T-B curve fitting with NN approximation in square lattice (c) (d) T-B curve fitting with NN approximation in triangular lattice | 26 |
| Fig. 3-5 | (a) (b) T-B curve fitting with NNNN approximation in square lattice (c) (d) T-B curve fitting with NNNN approximation in triangular lattice..... | 27 |
| Fig. 3-6 | The defect at the n th site coupling with the l th defect in the other PCW..... | 28 |
| Fig. 3-7 | The energy band structures and their electric field patterns of the defect modes of two coupled linear PCWs with both cases of remove | |

| | | |
|-----------|---|----|
| | and reduce rods in square lattice (a) (b) and triangular lattice (c) (d), which are split into two eigenmodes. The center lines are the defect of single PCW..... | 30 |
| Fig. 3-8 | The energy band structures and their electric field patterns of the defect modes of two coupled linear PCWs with both cases of remove and reduce rods in square lattice (a) (b) and triangular lattice (c) (d), which are split into two eigenmodes. The center lines are the defect of two PCWs..... | 31 |
| Fig. 3-9 | Photonic crystal directional coupler..... | 35 |
| Fig. 3-10 | A diagram of the fault in power ratio in usual PhC directional coupler..... | 35 |
| Fig. 3-11 | The band structure of two PCWs..... | 36 |
| Fig. 3-12 | The plot of the coupling length L as the function of frequency f | 37 |
| Fig. 3-13 | A directional coupler made by silicon rod array..... | 38 |
| Fig. 3-14 | The plot of the power ratio as the function of frequency f | 38 |
| Fig. 3-15 | A resonant ring coupler made by silicon rod array..... | 39 |
| Fig. 3-16 | (a) Forward wave of FDTD simulation of the ring design (b) backward wave of FDTD simulation of the ring design..... | 40 |
| Fig. 3-17 | The plot of the power ratio as the function of frequency f | 40 |
| Fig. 3-18 | (a) The spectrum of the width 5Λ of the resonant ring coupler (b) The spectrum of the width 7Λ of the resonant ring coupler..... | 41 |
| Fig. 3-19 | PCs WDM design..... | 42 |
| Fig. 3-20 | The plot of the coupling length L as the function of frequency f | 43 |
| Fig. 3-21 | FDTD simulated E-field at decoupled frequency and $\lambda_c = 1336$ | |

| | | |
|-----------|--|----|
| | nm..... | 44 |
| Fig. 3-22 | FDTD simulated E-field at decoupled frequency and $\lambda_B = 1312$ nm..... | 44 |
| Fig. 3-23 | FDTD simulated E-field at decoupled frequency and $\lambda_A = 1300$ nm..... | 45 |
| Fig. 3-24 | The plot of the power ratio $P1/P2$ and $P1/P3$ as the function of frequency f | 46 |
| Fig. 3-25 | The plot of the power ratio $P2/P1$ and $P2/P3$ as the function of frequency f | 46 |
| Fig. 3-26 | The plot of the power ratio $P3/P1$ and $P3/P2$ as the function of frequency f | 47 |



Chapter 1 Introduction

1-1 Background

During the past decade the use of photonic crystals (PhCs) has been studied and risen from an indistinct technology to a prominent field of research [1,2]. This is mainly because of their potential ability to well control the propagation of light. Eli Yablonovitch [3] and Sajeev John [4] initially predicted the idea that a periodic structure consisting of materials with different dielectric constants possesses bandgaps for certain ranges of the frequency, in much the same way as an electronic bandgap exists in semiconductor materials. Photonic crystal with defects can be found much more applications. Defects in photonic crystals means the points or places different from perfectly arrayed structures. Defects just like missing a point, line or dislocations can create defect modes within the photonic band gap. Using this property, photonic crystals can modify the spontaneous emission efficiency and the propagation of light, leading to novel applications in splitter, waveguides (Fig. 1-1), defect-mode light-emitters, electro-optical switch [5], Mach-Zehnder interferometer [6], and micro-cavity lasers (Fig. 1-2) [7–10], etc. This is why many scholars believe that the PhCs bring us a possible solution and unlimited vision of creating large-scale photonic integrated circuits (PICs) in the future and have done more and more studies on photonic crystals. Numbers of reports focusing on the design of PhC's devices in PICs have been published in the last few years [11].

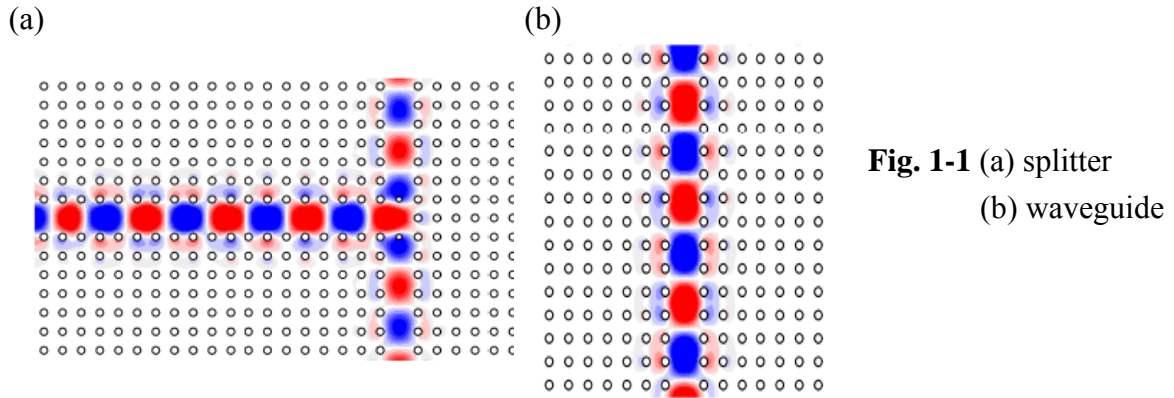


Fig. 1-1 (a) splitter
(b) waveguide

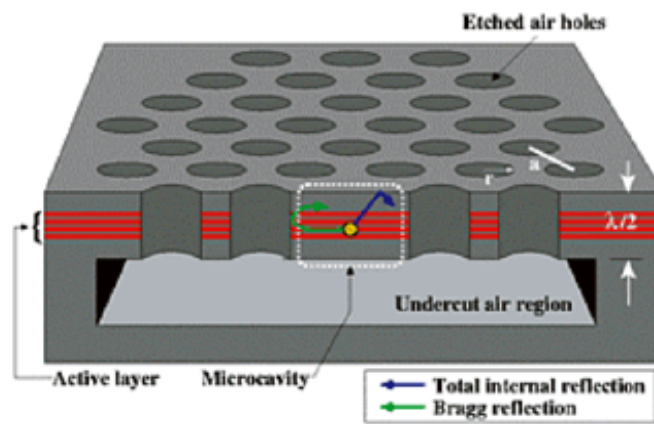


Fig. 1-2 Photonic-crystal micro-cavity laser

Two-dimension photonic crystals are regarded as the hottest topic nowadays, because they offer the possibility of fabricating high-Q cavities [12-13] and waveguide devices [14] on the scale of the wavelength in the semiconductor-based structures (i.e. GaAs/AlGaAs or SOI). Photonic integrated circuits of similar integration density so far only known as electronic VLSI (Very Large Scale Integrated Circuits) can be imagined. Photonic crystal waveguide (PCW) is an important basic element in PICs [15, 16] as important as the electric wire in the electric circuits. It is the key component of interconnect between optical circuits. Optical waveguiding in two-dimension photonic crystals is achieved by introducing line defects in the structure that is otherwise periodic in two dimensions.

When we take photonic crystal as basic structure of waveguide, another important characteristic of photonic crystal is its unusual dispersion property. Group velocity

dispersion of line defect in photonic crystal slabs is experimentally proved to be extremely large, and can be tuned via adjusting the widths of defects [17]. In conventional total internal reflection (TIR) waveguide, the bending angle for changing light propagation direction cannot be over 1° , otherwise the loss will be quite big. Different from the conventional waveguides, photonic crystal band gap (PBG) and large group velocity of PCWs can still keep well guiding the signal even if they form sharp-bend, as shown in Fig. 1-3.

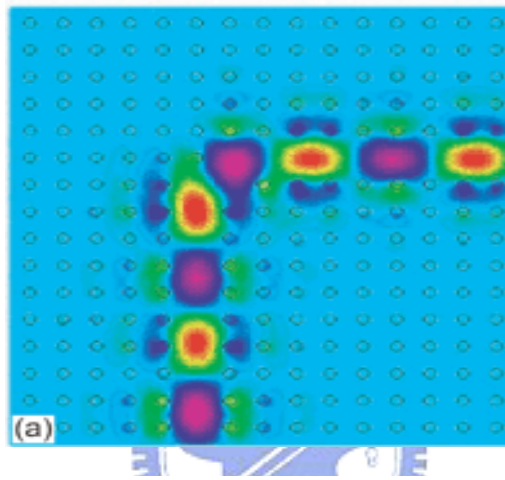


Fig. 1-3 Distribution of the real part of electric field in a 90° bend of the dielectric rods PCs. The red color shows positive amplitude of electric field and the blue for negative amplitude.

Two closely parallel waveguides can be used as a directional waveguide coupler [18-22]. A directional waveguide coupler is also one of key components for optical communication. They can be used as wavelength-selective power dividers, switches, modulators, etc. [23, 24] Besides, it might be desirable to decouple the two waveguides to minimize cross talk between them, for example, when envisioning closely packed photonic wires in integrated optical circuits [25].

Other phenomena of two-dimension PhCs had also been widely discussed, including coupling/decoupling, energy flow [26], and extremely low group velocity [27-28]. All of those researches make us getting closer and closer to entirely grasp this new technologies.

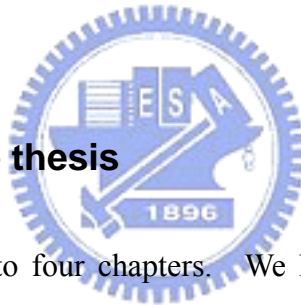
1-2 Motivation

In order to prepare for arrival of the next-generation optical communication, many scholars try to develop new optical devices which possess tiny scale, high efficiency, integrability and easy fabrication. Fortunately, people found some kinds of man-made materials called photonic crystals that make all our imagination realizable. By introducing different defects into perfect photonic crystals, many abilities such as wave-guiding, light-trapping, filtering, slowing light and light coupling could all be generated at will. With integrating such devices in a single chip, large photonic integrated circuits provide a wide view of future information technology. People even predict the coming of the photonic computer in the next ten years.

For optical communication systems used now, the size of the wavelength dependent power splitter is about hundreds of micrometer. If one can reduce the size of photonic crystal directional coupler devices to ten of micrometers, it should provide a great advantage for wavelength division multiplexing (WDM) systems. This provides the motivation to develop an effective numerical method for analyzing coupling between channel waveguides in a two-dimension photonic crystal. In the previous research, a photonic crystal waveguide is formed by a chain of point defects, so the waveguide can be regarded as a coupled-cavity waveguide (CCW), in which the energy can hop from a cavity to the neighbor one. The propagation of wave through a CCW is exactly the classical wave analog of the tight-binding (TB) method in solid state physics. It also indicates that there exists a large potential in designing various compact photonic devices by using the large dispersion of coupled mode splitting. According to this idea, we can do the design of PhC devices applying in optical communication with micrometer scale. In the following chapter, we will present two topics focusing on physical insight in PhC waveguides with tight-binding theory and optical devices

such as WDM based on photonic crystal with silicon rod array. In order to design WDM, we need to know the coupling length at each frequency. According to the coupling length formula $L=\pi/\Delta k$, we must know the value of Δk in order to calculate the coupling length. Although we can obtain a band structure through the plane wave expansion (PWE) method, it needs to extensive calculation to generate good resolution of dispersion curve, especially for the decoupling point of two identical photonic crystal waveguides (PCWs). By using the dispersion function derived from the tight-binding theory, we can well fit the calculated dispersion curves of the derived dispersion function. In turn, we can easily calculate the coupling length at corresponding frequency using the dispersion relation function. Therefore, few data of dispersion relation calculated from the PWE are enough to determine the dispersion function and the decoupling point.

1-3 Organization of the thesis



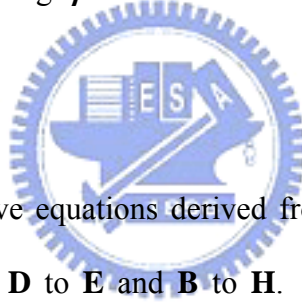
We divided this thesis into four chapters. We have narrated a brief statement to the background and history of the photonic crystal and also our research motivations in chapter 1. The main theory and numerical analysis methods we depended will put in chapter 2. After that, in the chapter 3 we will describe our approaches to the coupling problem between PCWs and our PhC optical device design and the simulation results. In the end, the final conclusion will be presented in chapter 4.

Chapter 2 Calculation Method and Theory

As same as all studies of the electromagnetism, analyses to the propagation of light in a photonic crystal also start with four macroscopic Maxwell's equations. In cgs units, they are

$$\begin{aligned} \nabla \cdot \mathbf{B} &= 0 & \nabla \times \mathbf{E} + \frac{1}{c} \frac{\partial \mathbf{B}}{\partial t} &= 0 \\ \nabla \cdot \mathbf{D} &= 4\pi\rho & \nabla \times \mathbf{H} - \frac{1}{c} \frac{\partial \mathbf{D}}{\partial t} &= \frac{4\pi}{c} \mathbf{J}, \end{aligned} \quad (2.1)$$

where \mathbf{E} and \mathbf{H} are the macroscopic electric and magnetic fields, \mathbf{D} and \mathbf{B} are the electric displacement and magnetic induction fields, and ρ and \mathbf{J} are free charge and current densities, respectively. Here we are concerned with the behavior of an electromagnetic wave in a source-free region where free charge ρ and free current \mathbf{J} in Eq. (2.1) are both zero.



2-1 Introduction

In order to solve the wave equations derived from Maxwell's equations, we need the constitution equations relating \mathbf{D} to \mathbf{E} and \mathbf{B} to \mathbf{H} . Since we do not deal with magnetic material, we assume the magnetic permeability μ is very close to unity and we may set $\vec{B}(\vec{r}, t) = \vec{H}(\vec{r}, t)$.

As for \mathbf{D} and \mathbf{E} , quite generally the components D_i of the displacement field are related to the electric field components E_i by the following power series [1]:

$$D_i = \sum_j \varepsilon_{ij} E_j + \sum_j k \chi_{ijk} E_j E_k + O(E^3). \quad (2.2)$$

To simplify the question, we make four assumptions. First we usually assume the field strengths are small enough so that we are in the linear regime. It means χ and all higher order terms can be ignored. Second, we assume the material is macroscopic and isotropic, so that $E(r, \omega)$ and $D(r, \omega)$ are related by a scalar dielectric constant $\varepsilon(r, \omega)$. Third, any explicit frequency dependence of the dielectric constant are also been ignored. The last

assumption is that we focus only on low-loss dielectrics, which means $\varepsilon(r)$ is treated as pure real. Hence, we have a brief expression relating \mathbf{D} and \mathbf{E} fields as

$$\mathbf{D}(r) = \varepsilon(r)\mathbf{E}(r). \quad (2.3)$$

With four assumptions above, the Maxwell's equations [Eq. (2.1)] become

$$\begin{aligned} \nabla \cdot \mathbf{H}(r, t) &= 0 & \nabla \times \mathbf{E}(r, t) + \frac{1}{c} \frac{\partial \mathbf{H}(r, t)}{\partial t} &= 0 \\ \nabla \cdot \varepsilon(r)\mathbf{E}(r, t) &= 0 & \nabla \times \mathbf{H}(r, t) - \frac{\varepsilon(r)}{c} \frac{\partial \mathbf{E}(r, t)}{\partial t} &= 0. \end{aligned} \quad (2.4)$$

The field functions \mathbf{E} and \mathbf{H} generally are both complicated functions of time and space, but thanks to the linearity of Maxwell's equation, it is convenient to look for solutions in form of harmonic fields:

$$\begin{aligned} \mathbf{H}(r, t) &= \mathbf{H}(r)e^{i\omega t} \\ \mathbf{E}(r, t) &= \mathbf{E}(r)e^{i\omega t} \end{aligned} \quad (2.5)$$

Because there is no free charge and current, the electromagnetic waves considered to be transverse. By substituting Eq. (2.5) into Eq. (2.4) we can obtain the following equations:

$$\Theta_E \bar{\mathbf{E}}(\bar{r}) \equiv \frac{1}{\varepsilon(\bar{r})} \nabla \times \{ \nabla \times \bar{\mathbf{E}}(\bar{r}) \} = \frac{\omega^2}{c^2} \bar{\mathbf{E}}(\bar{r}) \quad (2.6)$$

$$\Theta_H \bar{\mathbf{H}}(\bar{r}) \equiv \nabla \times \left\{ \frac{1}{\varepsilon(\bar{r})} \nabla \times \bar{\mathbf{H}}(\bar{r}) \right\} = \frac{\omega^2}{c^2} \bar{\mathbf{H}}(\bar{r}). \quad (2.7)$$

Solving Eqs. (2.6) and (2.7) is to solve the eigen-value problems, and Θ_H is a *Hermitian* operator. The eigenvectors $\mathbf{H}(\mathbf{r})$ and $\tilde{\mathbf{E}}(\mathbf{r})$ (where $\tilde{\mathbf{E}}(\mathbf{r}) = \sqrt{\varepsilon(\mathbf{r})}\mathbf{E}(\mathbf{r})$) are the field patterns of the harmonic modes, and the eigenvalues $(\frac{\omega}{c})^2$ are proportional to the square frequencies of those modes.

The Maxwell's equations are the most important kernel of following calculations (both PWE and FDTD) and analyses in the next chapter except only the tight-binding approximation by solid-state physics that we'll discuss later.

2-2 Plane-wave expansion method

Photonic crystals is a periodically arranged structure (i.e., its dielectric constant is periodic distributed), so we assume that the dielectric constant is real, isotropic, perfectly periodic with the spatial coordinate \vec{r} , and does not depend on frequency. Hence we can write its dielectric function as

$$\varepsilon(\vec{r}) = \varepsilon(\vec{r} + \vec{a}_i), \quad i = 1,2,3, \quad (2.8)$$

where $\{\vec{a}_i\}$ are the primitive lattice vectors of the photonic crystal. Because of the spatial periodicity, we introduce the primitive reciprocal lattice vectors $\{\mathbf{b}_i ; i=1,2,3\}$ and the reciprocal lattice vector can be defined as $\{\mathbf{G}\}$:

$$\mathbf{a}_i \cdot \mathbf{b}_j = 2\pi\delta_{ij}$$

and $\mathbf{G} = l_1\mathbf{b}_1 + l_2\mathbf{b}_2 + l_3\mathbf{b}_3,$ (2.9)

where $\{l_i\}$ are arbitrary integers and δ_{ij} is the Kronecker's delta function. We can expand

$\varepsilon^{-1}(\vec{r})$ into Fourier series as

$$\frac{1}{\varepsilon(r)} = \sum_G \kappa(G) \exp(iG \cdot r). \quad (2.10)$$

Because ε is a periodic function of the spatial coordinate r , we can apply Bloch's theorem to Eqs. (2.6) and (2.7). $E(r)$ and $H(r)$ are thus characterized by a wave vector k in the first Brillouin zone and a band index n and expressed as

$$E(r) = E_{kn}(r) = u_{kn}(r)e^{ik \cdot r} \quad (2.11)$$

$$H(r) = H_{kn}(r) = v_{kn}(r)e^{ik \cdot r}, \quad (2.12)$$

where $u_{kn}(r)$ and $v_{kn}(r)$ are periodic vectorial functions:

$$u_{kn}(r + a_i) = u_{kn}(r) \quad (2.13)$$

$$v_{kn}(r + a_i) = v_{kn}(r), \quad \text{for } i = 1,2,3. \quad (2.14)$$

These periodic functions can be expanded in Fourier series as $\varepsilon^{-1}(r)$ in Eq. (2.10). The

two Fourier expansions of the fields can be derived as the following form of the eigenfunctions:

$$E_{kn}(r) = \sum_G E_{kn}(G) \exp\{i(k+G) \cdot r\} \quad (2.15)$$

$$H_{kn}(r) = \sum_G H_{kn}(G) \exp\{i(k+G) \cdot r\}. \quad (2.16)$$

The expansion coefficients in reciprocal lattice space, i.e., $E_{kn}(G)$ and $H_{kn}(G)$ are denoted by the same symbols as the original ones in real space. Substituting Eq. (2.15), (2.16), (2.11) and (2.12) into (2.6) and (2.7), we obtain the following eigenvalue equations for the expansion coefficients $\{E_{kn}(G)\}$ and $\{H_{kn}(G)\}$:

$$-\sum_{G'} \kappa(G-G') \{(k+G') \times (k+G') \times E_{kn}(G')\} = \frac{\omega_{kn}^2}{c^2} E_{kn}(G) \quad (2.19)$$

$$-\sum_{G'} \kappa(G-G') (k+G) \times \{(k+G') \times H_{kn}(G')\} = \frac{\omega_{kn}^2}{c^2} H_{kn}(G), \quad (2.20)$$

where ω_{kn} denotes the eigen-angular frequency of $E_{kn}(r)$ and $H_{kn}(r)$. The vector electromagnetic field in the 2D photonic lattice can be decomposed into two independent polarization components, i.e., an E polarization (TM mode) for which the electric field is parallel to the rod axis (E_z only), and an H polarization (TE mode) for which the magnetic field is parallel to the rod axis (H_z only). In two-dimensional photonic crystals, Eq. (2.19) and Eq. (2.20) reduce to

$$\sum_{G'} |k+G'| |k+G| \varepsilon^{-1}(G-G') E_{kn}(G') = \frac{\omega_{kn}^2}{c^2} E_{kn}(G), \quad (2.21)$$

where Eq. (2.21) is the master equation of TM mode. Similarly, the master equation of TE mode can be written as

$$\sum_{G'} (k+G') \square (k+G) \varepsilon^{-1}(G-G') H_{kn}(G') = \frac{\omega_{kn}^2}{c^2} H_{kn}(G). \quad (2.22)$$

For the photonic band calculating, the expansion coefficients $\{\varepsilon^{-1}(G)\}$ in Eq. (2.10) is necessary to be calculated by the plane-wave expansion method. The inverse Fourier transform gives

$$\varepsilon^{-1}(G) = \frac{1}{V} \int_V dr \varepsilon^{-1}(r) \exp(-iG \cdot r), \quad (2.23)$$

where V is the volume of the unit cell of the photonic crystal. In general, this integral should be numerically evaluated by FFT method. However, if the shapes of the dielectric components in the unit cell are simple enough, we can calculate it analytically.

2-3 Finite-difference time domain method (FDTD) [29]

The finite-difference time-domain method is introduced by Yee in 1966 [30]. During the 1970s and 1980s, several defense agencies working in the areas motivated large-scale solutions of Maxwell's equations. The entire field of computation electrodynamics is shifting rapidly in high-speed communications and computing. In 1990, engineers in the general electromagnetic community became aware of the modeling capabilities afforded by FDTD and related techniques, and the interest in this area has expanded well beyond defense technology. The main reason to introduce FDTD method to solve photonic crystal is that when the structure is too complex, it is hard to solve Maxwell's equation in frequency domain. FDTD provide a straight forward way to solve it in time domain. With this method, we can see the field distribution in photonic crystals. In addition, there are several advantages in FDTD method. First, FDTD is accurate and robust. The sources of error are well known. Second, being a time domain technology, FDTD treats impulsive behavior and nonlinear behavior naturally. Third, FDTD uses no linear algebra. Being a fully explicit computation, FDTD avoids the difficulties with linear algebra that limit the size of frequency-domain integral-equation.

When the differential forms of Maxwell's equations are examined, it can be seen that the time derivative of the E field is related to the curl of the H field ($\nabla \times H$). This can be simplified to state that the rate of the change in the E field (the time derivative) depends on the change in the H field across space (the curl). The results in the basic FDTD equations are that the new value of the E field is related to the old value of the E field (hence the

difference in time) and the difference of old values of the H fields on either side of the E field point in space. Naturally, this is a simplified description as illustrated in Fig. 2-1.

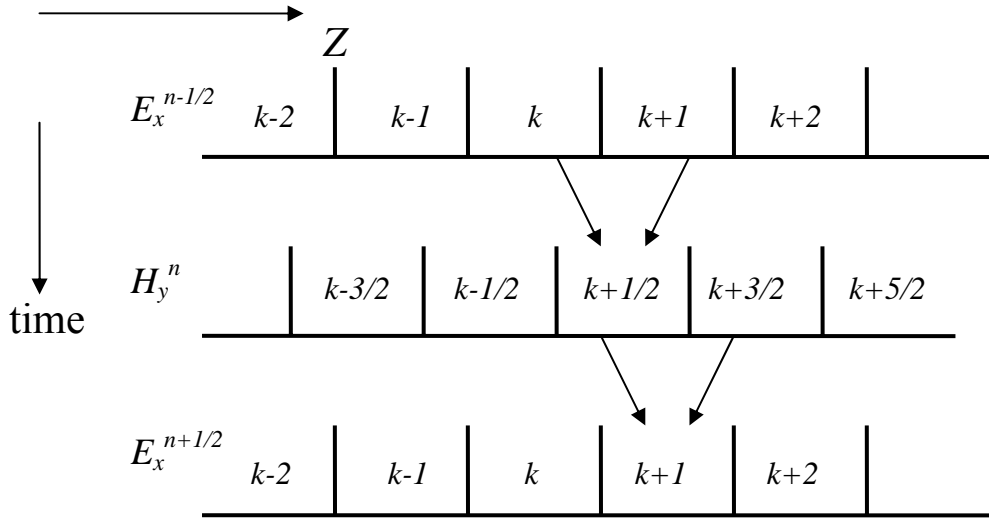


Fig. 2-1 Interleaving of the E and H fields in space and time in the FDTD formulation.



2-3.1 FDTD method in One-dimensional case

Now we will start with simple one-dimensional differential equations. The time-dependent Maxwell's curl equations in free space are

$$\frac{\partial E}{\partial t} = \frac{1}{\epsilon_0} \nabla \times H \quad (2.24)$$

$$\frac{\partial H}{\partial t} = -\frac{1}{\mu_0} \nabla \times E. \quad (2.25)$$

Here E and H are vectors in three dimensions. When we consider only in one dimension case, E and H simply have E_x and H_y components, so Eq. (2.24) and (2.25) become

$$\frac{\partial E_x}{\partial t} = -\frac{1}{\epsilon(r)\epsilon_0} \frac{\partial H_y}{\partial z} \quad (2.26)$$

$$\frac{\partial H_y}{\partial t} = -\frac{1}{\mu_0} \frac{\partial E_x}{\partial z}. \quad (2.27)$$

Above equations mean the electric field oriented in the x direction and the magnetic field

oriented in the y direction both traveling in the z direction. Taking the central difference approximation for both the temporal and spatial derivatives gives

$$\frac{E_x^{n+1/2}(k) - E_x^{n-1/2}(k)}{\Delta t} = -\frac{1}{\varepsilon(r)\varepsilon_0} \frac{H_y^n(k+1/2) - H_y^n(k-1/2)}{\Delta z} \quad (2.28)$$

$$\frac{H_y^{n+1}(k+1/2) - H_y^n(k+1/2)}{\Delta t} = -\frac{1}{\mu_0} \frac{E_x^{n+1/2}(k+1) - E_x^{n+1/2}(k)}{\Delta z}. \quad (2.29)$$

In these two equations, “ n ” actually means a time $t = \Delta t \cdot n$. The term “ $n+1$ ” means one time step later; “ k ” actually means the distance $z = \Delta z \cdot k$. The formula of Eqs. (2.28) and (2.29) assume that \mathbf{E} and \mathbf{H} fields are interleaved in both space and time. \mathbf{H} uses the arguments $k+1/2$ and $k-1/2$ to indicate that the \mathbf{H} field values are assumed to be located between the \mathbf{E} field values. Similarly, superscript $n+1/2$ or $n-1/2$ indicates that it occurs slightly after or before n , respectively. Eq. (2.28) and (2.29) can be rearranged as

$$E_x^{n+1/2}(k) = E_x^{n-1/2}(k) - \frac{\Delta t}{\varepsilon(r)\varepsilon_0 \cdot \Delta z} [H_y^n(k+1/2) - H_y^n(k-1/2)] \quad (2.30)$$

$$H_y^{n+1}(k+1/2) = H_y^n(k+1/2) - \frac{\Delta t}{\mu_0 \cdot \Delta z} [E_x^{n+1/2}(k+1) - E_x^{n+1/2}(k)]. \quad (2.31)$$

The calculations are interleaved in both space and time. This is the fundamental paradigm of the finite-difference time-domain (FDTD) method. Eqs. (2.30) and (2.31) are very similar, but because ε_0 and μ_0 differ by several orders of magnitude. This is circumvented by making the following change of variables:

$$\tilde{E} = \sqrt{\frac{\varepsilon_0}{\mu_0}} E. \quad (2.32)$$

Substituting (2.32) into (2.30) and (2.31) gives

$$\tilde{E}_x^{n+1/2}(k) = \tilde{E}_x^{n-1/2}(k) - \frac{1}{\varepsilon\sqrt{\varepsilon_0\mu_0}} \frac{\Delta t}{\Delta z} [H_y^n(k+1/2) - H_y^n(k-1/2)] \quad (2.33)$$

$$H_y^{n+1}(k+1/2) = H_y^n(k+1/2) - \frac{1}{\sqrt{\varepsilon_0\mu_0}} \frac{\Delta t}{\Delta z} [\tilde{E}_x^{n+1/2}(k+1) - \tilde{E}_x^{n+1/2}(k)]. \quad (2.34)$$

If the cell size Δz is chosen, the time step Δt can be determined by

$$\Delta t \geq \frac{\Delta z}{2 \cdot c_0} \quad (2.35)$$

where c_0 is the light speed in free space. The reason why we determined the time step Δt to Eq. (2.30) related to the stability of the FDTD method. An electromagnetic wave propagating in free space cannot go faster than the speed of light. To propagate a distance of one cell Δz needs a minimum time of $\Delta t = \frac{\Delta z}{c_0}$. When we get to two-dimensional

simulation, we have to allow for the propagation in the diagonal direction, which brings the time requirement to $\Delta t = \frac{\Delta z}{\sqrt{2}c_0}$. Obviously, three-dimensional simulation requires

$\Delta t = \frac{\Delta z}{\sqrt{3}c_0}$. This is summarized by the well-known ‘‘Courant Condition’’ [31, 32]:

$$\Delta t \leq \frac{\Delta z}{\sqrt{d} \cdot c_0}, \quad (2.36)$$

where d is the dimension of the simulation. Hence we will determine Δt in Eq. (2.37).

This is not necessarily the best formula! Therefore,

$$\frac{1}{\sqrt{\epsilon_0 \mu_0}} \frac{\Delta t}{\Delta z} = c_0 \cdot \frac{\Delta z / 2 \cdot c_0}{\Delta z} = \frac{1}{2} \quad (2.37)$$

Substituting (2.35) into (2.33) and (2.34), those equations become

$$\tilde{E}_x^{n+1/2}(k) = \tilde{E}_x^{n-1/2}(k) - \frac{0.5}{\epsilon} (H_y^n(k+1/2) - H_y^n(k-1/2)) \quad (2.38)$$

$$H_y^{n+1}(k+1/2) = H_y^n(k+1/2) - 0.5[\tilde{E}_x^{n+1/2}(k+1) - \tilde{E}_x^{n+1/2}(k)] \quad (2.39)$$

Besides the last two iterative equations, we still need to add incident wave source condition and absorbing boundary condition. It is a great subject in dealing with the wave source condition. For simplicity, we divide it into two categories in 1-D case: hard source and soft source. In a hard source, a propagation wave will see that value and be reflected, because the hard value of E_x looks like a metal wall to FDTD. However a soft source is added to E_x at a certain point and a propagating pulse will just pass through. In calculating

photonic crystal, we must consider the field scattering from the material. Therefore we use a soft source.

$$\begin{aligned} pulse &= \sin(2\pi f * dt * t) \\ E_x &= E_x + pulse \end{aligned} \quad (2.40)$$

In order to keep outgoing E and H fields from being reflected by the calculation boundary and back into the problem space, so the absorbing boundary conditions (ABC) are necessary to consider. The fields at the edge must be propagating outward. In one time step of the FDTD algorithm it travels

$$distance = c_0 \cdot \Delta t = c_0 \cdot \frac{\Delta x}{2 \cdot c_0} = \frac{\Delta x}{2}. \quad (2.41)$$

This equation basically explains that it takes two time steps for a wave front to cross one cell.

So a common sense approach tells us that an ABC might be

$$\begin{aligned} E_x^n(0) &= E_x^{n-2}(1) \\ E_x^n(k) &= E_x^{n-2}(k-1), \end{aligned} \quad (2.42)$$

where 0 and k are the end points and n is a time step. Simply store a value of $E_x(1)$ two time steps before in $E_x(0)$. Boundary conditions such as these have been implemented at both ends of the E_x array. Below are the examples of C computer code in one-dimensional absorbing boundary conditions. Additional parameters are used to store the boundary value for two time steps during the calculation loop.

$$\begin{aligned} ex[0] &= ex_low_m2; \\ ex_low_m2 &= ex_low_m1; \\ ex_low_m1 &= ex[1]; \\ \\ ex[KE-1] &= ex_high_m2; \\ ex_high_m2 &= ex_high_m1; \\ ex_high_m1 &= ex[KE-2]; \end{aligned} \quad (243)$$

2-3.2 Two-dimensional photonic crystal formulation and perfectly matched layer (PML) boundary condition

We start again with the normalized Maxwell's equations:

$$\frac{\partial \tilde{D}}{\partial t} = \frac{1}{\sqrt{\varepsilon_0 \mu_0}} \nabla \times H \quad (2.45)$$

$$\tilde{D}(\omega) = \varepsilon_r(\omega) \cdot \tilde{E}(\omega) \quad (2.46)$$

$$\frac{\partial H}{\partial t} = -\frac{1}{\sqrt{\varepsilon_0 \mu_0}} \nabla \times \tilde{E}. \quad (2.47)$$

where $\tilde{E} = \sqrt{\frac{\varepsilon_0}{\mu_0}} \bar{E}$ and $\tilde{D} = \frac{1}{\sqrt{\varepsilon_0 \mu_0}} \bar{D}$. In two dimension cases, there exist two groups of

six different fields. One is the transverse magnetic (TM) mode, which is composed of \tilde{E}_z , H_x , and H_y . Another is the transverse electric (TE) mode, which is composed of \tilde{E}_x , \tilde{E}_y , and H_z . In TM mode, therefore, Eq. (2.44) ~ (2.47) are reduced to

$$\frac{\partial D_z}{\partial t} = \frac{1}{\sqrt{\varepsilon_0 \mu_0}} \left(\frac{\partial H_y}{\partial x} - \frac{\partial H_x}{\partial y} \right) \quad (2.48)$$

$$D_z(\omega) = \varepsilon_r(\omega) \cdot E_z(\omega) \quad (2.49)$$

$$\frac{\partial H_x}{\partial t} = -\frac{1}{\sqrt{\varepsilon_0 \mu_0}} \frac{\partial E_z}{\partial y} \quad (2.50)$$

$$\frac{\partial H_y}{\partial t} = \frac{1}{\sqrt{\varepsilon_0 \mu_0}} \frac{\partial E_z}{\partial x}. \quad (2.51)$$

The two-dimensional systemic interleaving of the calculated fields is more complex than one dimension. That is illustrated in Fig. 2-2 below.

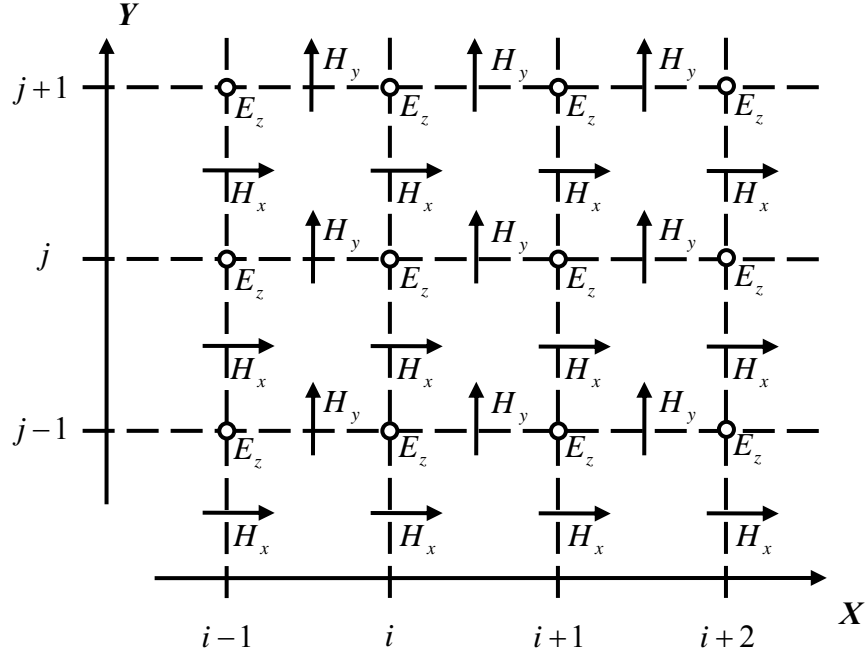


Fig. 2-2 Interleaving of the E and H fields for the two-dimensional TM formulation.

Put Eqs. (2.48), (2.50) and (2.51) into the finite difference scheme, and take equivalent incremental step in x and y direction, these equations become

$$\begin{aligned} \frac{D_z^{n+1/2}(i, j) - D_z^{n-1/2}(i, j)}{\Delta t} &= \frac{1}{\sqrt{\epsilon_0 \mu_0}} \left(\frac{H_y^n(i+1/2, j) - H_y^n(i-1/2, j)}{\Delta x} \right) \\ &\quad - \frac{1}{\sqrt{\epsilon_0 \mu_0}} \left(\frac{H_x^n(i, j+1/2) - H_x^n(i, j-1/2)}{\Delta x} \right) \end{aligned} \quad (2.52)$$

$$\frac{H_x^{n+1}(i, j+1/2) - H_x^n(i, j+1/2)}{\Delta t} = -\frac{1}{\sqrt{\epsilon_0 \mu_0}} \frac{E_z^{n+1/2}(i, j+1) - E_z^{n+1/2}(i, j)}{\Delta x} \quad (2.53)$$

$$\frac{H_y^{n+1}(i+1/2, j) - H_y^n(i+1/2, j)}{\Delta t} = \frac{1}{\sqrt{\epsilon_0 \mu_0}} \frac{E_z^{n+1/2}(i+1, j) - E_z^{n+1/2}(i, j)}{\Delta x}. \quad (2.54)$$

We have briefly mentioned the issue of absorbing boundary conditions (ABCs) in discussion of one dimension. In the two-dimensional simulations, the program contains two-dimensional matrices for the values of all the fields (i.e. d_z , e_z , h_x and h_y). Assume we

are simulating a wave generated from a point source propagating in the free space. As the wave propagates outward, it will eventually come to the edge of the allowable space, which is dictated by how the matrices have been dimensioned in the program. If we had done nothing about this, reflections would be produced and would go back the problem space. Then we will have no way to differentiate between the real wave and the reflected wave. This is why the ABCs must exist. The most effective ABCs is the perfectly matched layer (PML) developed by Berenger [32]. How PML works can be easily understood by the following description. If a wave propagating in medium A and it impinges upon medium B, the amount of reflection can be determined by the intrinsic impedances of two media

$$\Gamma = \frac{\eta_A - \eta_B}{\eta_A + \eta_B}, \quad (2.55)$$

where the impedance is $\eta = \sqrt{\frac{\mu}{\epsilon}}$. If μ changed with ϵ so η still remained a constant, Γ would be zero and no reflection will occur. But this is still helpless to our problem, because waves will continue propagating in the new medium. We really want is a medium that is also lossy so the wave will decrease before it hits the boundary. Hence we mark both ϵ and μ of complex due to their imaginary parts causing decay.

To simulate a plane wave propagating in a 2D FDTD program, the space of problem will be divided into two regions, the *total field* and the *scattered field* (Fig. 2-3). There are two reasons for doing this: (1) The propagating plane wave should not interact with the absorbing boundary conditions; (2) the load on the absorbing boundary conditions should be minimized. These boundary conditions are not perfect. By subtracting the incident field, the amount of the radiating field hitting the boundary is minimized, thereby reducing the calculation error.

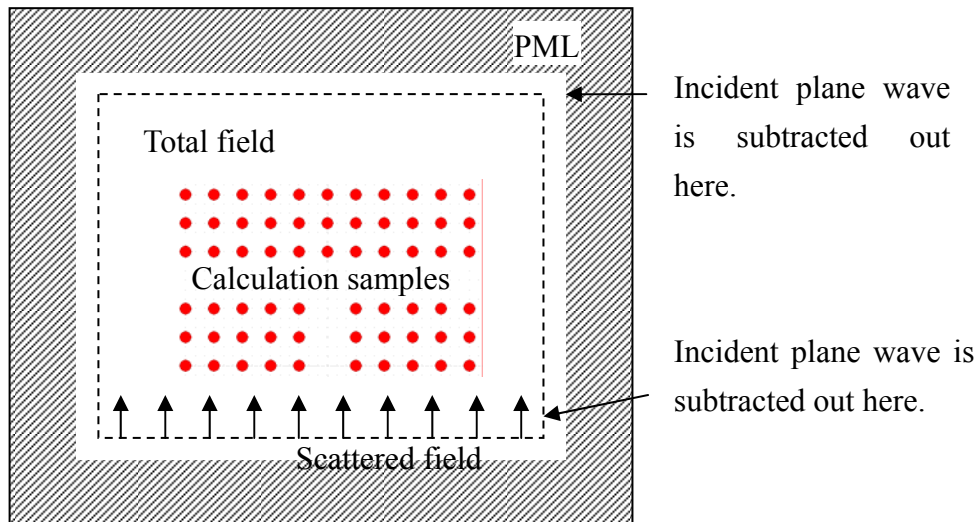


Fig. 2-3 Total field/scattered field of the two-dimensional problem space.

2-4 Tight binding method in solid state physics

In the later discussion of the coupling between the photonic crystal waveguides we will apply the tight binding approximation to support our argument. So we here do a simple introduction of what is the tight binding method and its meaning in solid state physics [33].

In atoms the electrons are *tightly* bound to their nuclei. If the atoms are so close that their separations become comparable to the lattice constant in solids, their wave functions will overlap each other. If we consider only two atoms, their combined wave functions are $\psi_A \pm \psi_B$. The electron energy of state $\psi_A + \psi_B$ is lower than one of state $\psi_A - \psi_B$. After they approach to each other, the Coulomb force between nucleuses and electrons can cause the energy level splitting and becomes energy band. The approximation method to obtain the energy band structure by calculating the free atomic wave functions is called tight binding approximation (TB) or linear combination of atomic orbitals (LCAO). In covalently bonded semiconductors the valence electrons are concentrated mainly in the bonds. Therefore the wave functions of valence electrons should be very similar to bonding orbitals

found in molecules. In addition to being a good approximation for calculating the valence bond structure, the TB method has the advantage that the band structure can be defined in terms of a small number of overlap parameters. The overlap parameters have a simple physical interpretation as representing interactions between electrons of adjacent atoms.

Assume that an electron with ground state $\varphi(r)$ exercises within a single atom's potential $U(r)$, where $\varphi(r)$ denotes as the s state. It is too complex if we solve the energy band problem by using degenerated atomic energy levels. Therefore, we assume that the influence between two atoms is quite small, and then the wave function can be expanded as following :

$$\psi_k(r) = \sum_j C_{kj} \varphi(r - r_j). \quad (2.56)$$

If $C_{k,j} = N^{-1/2} e^{ik \cdot r_j}$ in Eq. (2.56) is for a crystal with N atoms, the Bloch form of the above equation can be expressed as

$$\psi_k(r) = N^{-1/2} \sum_j \exp(ik \cdot r) \varphi(r - r_j), \quad \psi_k(r+T) = \exp(ik \cdot T) \psi_k(r), \quad (2.57)$$

where T is the primitive vector connecting two lattice points. To calculate the 1st level energy by doing the Hamiltonian matrix diagonalization as follow:

$$\langle k | H | k \rangle = N^{-1} \sum_j \sum_m \exp[ik \cdot (r_j - r_m)] \langle \varphi_m | H | \varphi_j \rangle, \quad (2.58)$$

where $\varphi_m \equiv \varphi(r - r_m)$. Let $\rho_m = r_m - r_j$, then

$$\langle k | H | k \rangle = \sum_m \exp(ik \cdot \rho_m) \int dV \varphi^*(r - \rho_m) H \varphi(r). \quad (2.59)$$

In Eq. (2.59), we do the integration to only an atom and other atoms nearby which are tied up by ρ . We can rewrite it as:

$$\int dV \varphi^*(r) H \varphi(r) = -a; \quad \int dV \varphi^*(r - \rho) H \varphi(r) = -\gamma \quad (2.60)$$

To set $\langle k | k \rangle = 1$, the 1st level energy is

$$\langle k | H | k \rangle = -a - \gamma \sum_m \exp(ik \cdot \rho_m) = \varepsilon_k. \quad (2.61)$$

The relation between overlapping energy γ and atomic spacing ρ in two hydrogen atoms which are both in the 1s state can be clearly calculated. Using the Rydberg-energy unit, $Ry = me^4 / 2\hbar^2$, we have

$$\gamma(Ry) = 2(1 + \rho/a_0) \exp(-\rho/a_0). \quad (2.62)$$

Considering to a simple cubic structure, the positions of the closest atoms are

$$\rho_m = (\pm a, 0, 0); (0, \pm a, 0); (0, 0, \pm a). \quad (2.63)$$

So Eq. (2.61) becomes

$$\varepsilon_k = -a - 2\gamma(\cos k_x a + \cos k_y a + \cos k_z a). \quad (2.64)$$

Other example likes the **fcc** structure which has twelve closest atoms and its band structure can be described as

$$\varepsilon_k = -a - 4\gamma(\cos \frac{1}{2} k_y a \cos \frac{1}{2} k_z a + \cos \frac{1}{2} k_z a \cos \frac{1}{2} k_x a + \cos \frac{1}{2} k_x a \cos \frac{1}{2} k_y a). \quad (2.65)$$

Hence the tight-binding approximation method provides a very simple way to do the atomic energy band structure analysis. This way can also be applied to discussion of the small coupling effect inside a photonic crystal coupled-cavities waveguides (CCWs).

Chapter 3 Simulation and Discussion

In this chapter, we will bring up a series of research focusing on both waveguide properties and 2-D photonic crystals devices. Two subjects have been discussed in the following text, including tight-binding theory of coupling behavior in the PhC waveguides and WDM design using resonant ring devices. Many related and additional points have also been analyzed.

3-1. Long-range interaction of defect modes between coupled identical photonic crystal waveguides

When two identical photonic crystal waveguides (PCWs) are placed close to each other, a “band-crossing” property could be found in the dispersion relation. We use MIT photonic band code to investigate the band structures with void and reduced line-defects in square and triangular lattices and coupling between two PCWs in silicon rod array. By using the tight-binding (TB) approximation, we fit the dispersion curves very well and accurately define the crossing point of dispersion curves.

3-1.1 Single line defect photonic crystal waveguides and tight-binding approximation

The PCW couplers consist of plural adjacent PCWs in which the guided modes are overlapped, resulting the splitting of dispersion curves. That is in common with its counterpart built with conventional optical waveguides. However, there is certain fundamental dissimilarity between these two categories of couplers. One remarkable example is the decoupling of the adjacent waveguides. Decoupling occurs where the dispersion curves of the split guided modes cross, namely the degeneracy has not be

removed at a certain frequency. To generate decoupling is an exhausting task to conventional waveguides, but a direct effect for PCWs [35-37].

Typically, the dispersion curves of the PCW couplers can be obtained numerically from the solutions of Maxwell's equations by the plane wave expansion (PWE) method [38]. However, the PWE does not provide enough insights to the coupling mechanism of PCWs. Also, there are very few literatures discussing this mechanism. In this thesis, we explain the PCW coupling with the long-range interactions among the eigenmodes of individual defects and derive the evolution equation of the guided modes. The split of the dispersion curves is attributed to the cross-waveguide coupling to the nearest neighboring (NN) defects and the next NN defects in the second PCW. The dispersion curves cross due to the cancellation of these two couplings, causing the decoupling of the PCWs.

A point defect, acts as an optical resonator (cavity), can be created by introducing a single defect into a photonic crystal that locally trap photons with a certain frequency inside the defect volume (Fig. 3-1(a)). The coupled cavity waveguide (also referred to as coupled resonator optical waveguide) composed of well-separated defects in PhC (Fig. 3-1(b)) has been proposed and demonstrated recently [39, 40]. It is assumed the defects are weakly coupled due to the overlapping of the individual evanescent eigenmodes (here referred to as defect modes) and the dispersion relation can be obtained by the formalism developed from the tight-binding (TB) approximation in solid state physics (Fig. 3-2). Only the couplings with the nearest neighboring (NN) defects are taken into account in this approximation as the defect modes are localized in the defect sites. The defects beyond the NN ones are ignored.

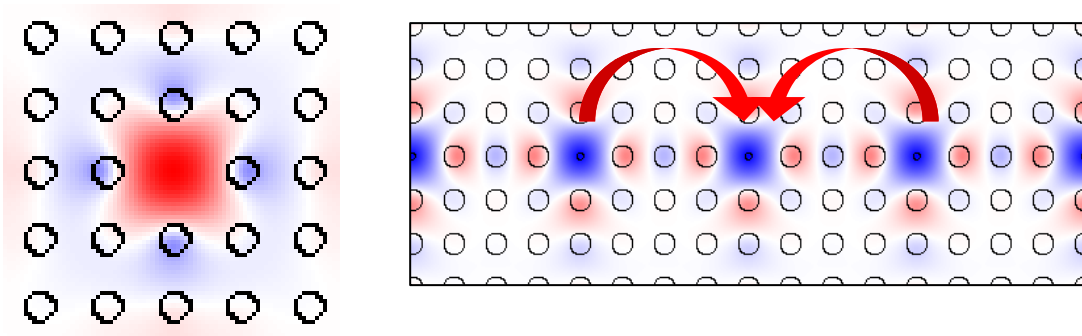


Fig. 3-1 (a) A single point defect, in which the photon in resonance frequency is trapped inside the point defect. (b) A diagram of coupled cavity waveguide (CCW).

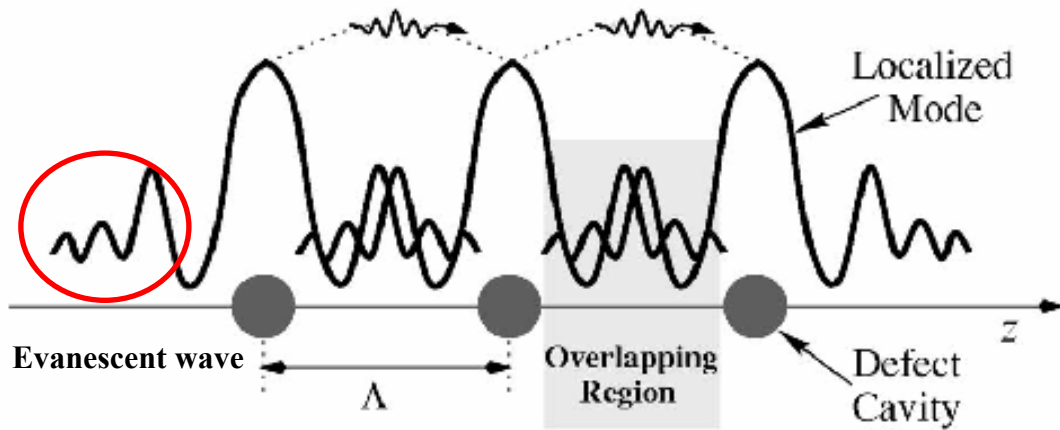


Fig. 3-2 Schematics of propagation of photons by the coupled evanescent defect modes.

Conceivably, a PCW can be regarded as a chain of consecutive defects, and the dispersion relations of the guided modes result from the superposition of longitudinal shifted defect modes. The coupling concept of the TB approximation is borrowed to model the dispersion relation in PCWs. Notably, the consecutive defects are still too close and the coupling beyond the NN defects is significant, which cannot be ignored in the evolution equation [41]. As the couplings to the remote defects are taken into account, the evolution equation extended from the TB approximation can be written as

$$i \frac{\partial}{\partial t} u_n = (w_0 + \alpha) u_n + \sum_{l=1} c_{nl} (u_{n+l} + u_{n-l}) \quad (3-1)$$

u_n represents the Bloch function at site n , w_0 is the resonant frequency of a single cavity, α is a small shift (arising from the presence of neighboring defect) in the eigenfrequency of the single point defect and c_{nl} is the coupling coefficient of the defect at site n with the l -th neighboring defects as illustrated in Fig. 3-3.

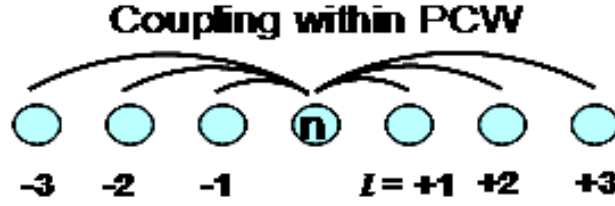


Fig. 3-3 The defect at site n coupling with the l th neighboring defects

Let $u_n(t) = u_0 \exp(ikna - iw_1 t)$, where k is the propagating constant, a is the lattice constant, and w_1 is the eigenfrequency of the single PCW. By substituting $u_n(t)$ into Eq. (3.1), we obtained the dispersion curve as

$$w_1 = w_0 + \alpha + \sum_{l=1} 2 c_{nl} \cos(lka) \quad (3-2)$$

The formula is applied to fit the dispersion curve of a single PCW derived from PWE. Two-dimensional (2D) PhCs consisting of a triangular lattice and a square lattice of dielectric rods with the lattice constant a in air were considered. Assume the PCW is formed by a line defect of void ($R_d=0a$) and reduced rods ($R_d=0.1a$) in a two dimensional PhC of both array of circular rods. Let the dielectric constant of the rod is 12 and the radius of the rod is $0.2a$. The dispersion curves derived from PWE (the dotted curve in Fig. 3-4) is fitted with Eq. (3-2) (the dash curve) as only the couplings with NN defects ($l = 1$) are involved. Obviously, the NN couplings are insufficient to accurately determine the dispersion curve, and the mode functions in a

PCW appear not well-localized. The curve is well fitted as long as the long-range couplings up to the third NN defects are taken into account, presented as the solid curve in Fig. 3-5. Therefore, Eq. (2) is recast as

$$w_1 = \Omega + 2 c_{n1} \cos(ka) + 2 c_{n2} \cos(2ka) + 2 c_{n3} \cos(3ka), \quad (3-3)$$

where Ω is the sum of w_0 and α . c_{n1} , c_{n2} , and c_{n3} are the TB parameters determined from splitting of several coupled cavities or the width of defect band. Equation (3.3) states the different strength of each evanescent waves coupling to the neighbors. Each fitting parameters in different orders are shown in Table 3-1 below.

| Lattice type | Defect type | Ω | $2c_{n1}$ | $2c_{n2}$ | $2c_{n3}$ |
|--------------|-------------|----------|-----------|------------|-------------|
| Square | reduced | 0.322156 | 0.0574397 | | |
| | | 0.32164 | 0.0572285 | 0.00825559 | 0.00179545 |
| | void | 0.372517 | 0.0737741 | | |
| | | 0.375729 | 0.0802634 | 0.00755291 | 0.000129329 |
| Triangular | reduced | 0.331878 | 0.0396954 | | |
| | | 0.331622 | 0.0396419 | 0.00409485 | 0.000454774 |
| | void | 0.393989 | 0.0585895 | | |
| | | 0.394934 | 0.0606635 | 0.00280332 | 0.000899578 |

Table 3-1 Fitting curve function of a single PCW

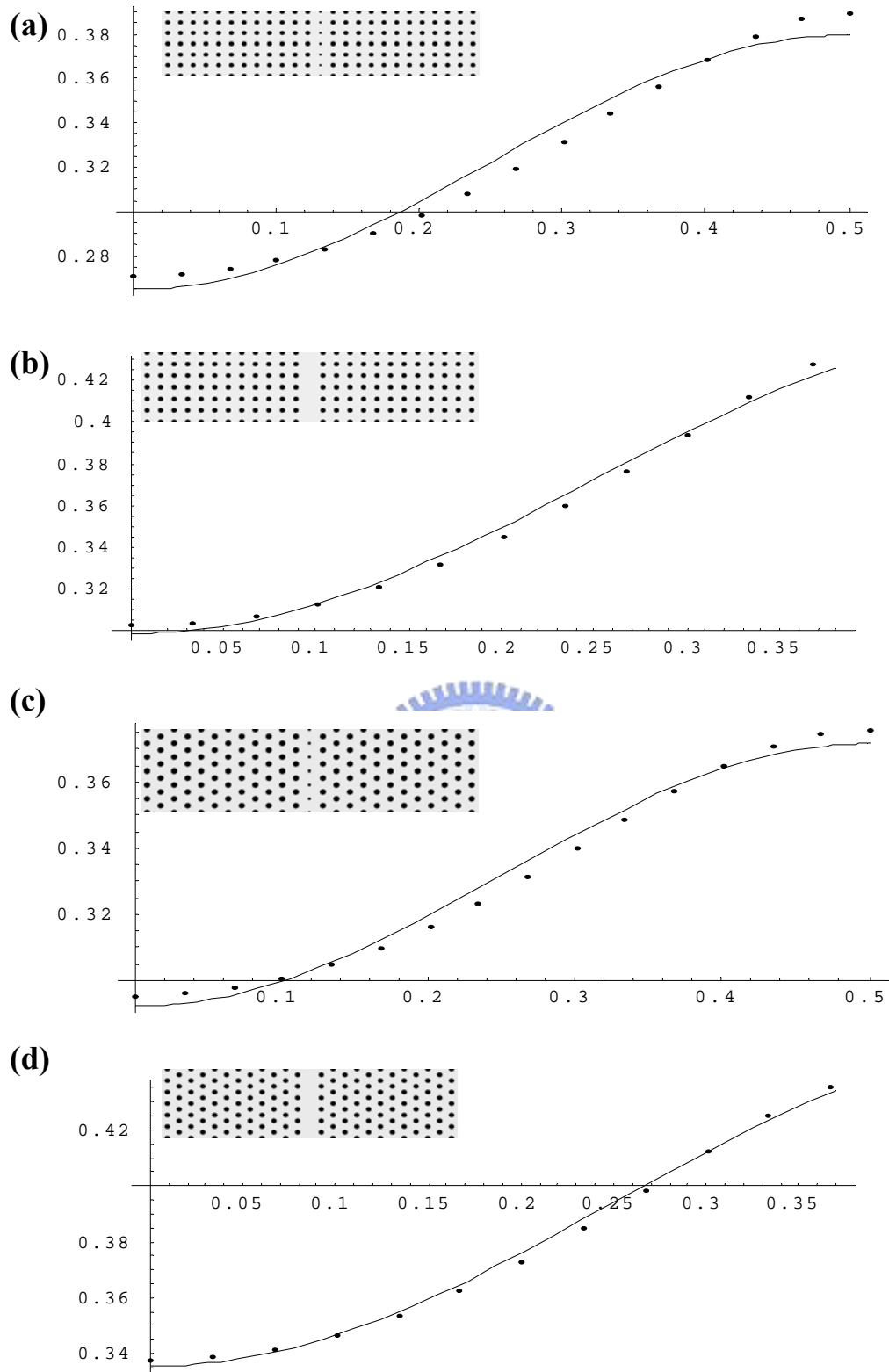


Fig. 3-4 (a) (b) The dispersion of the reduce and remove line-defect mode in square lattice and the fitting curve with NN approximation. (c) (d) The dispersion of the reduce and remove line-defect mode in triangular lattice and the fitting curve with NN approximation.

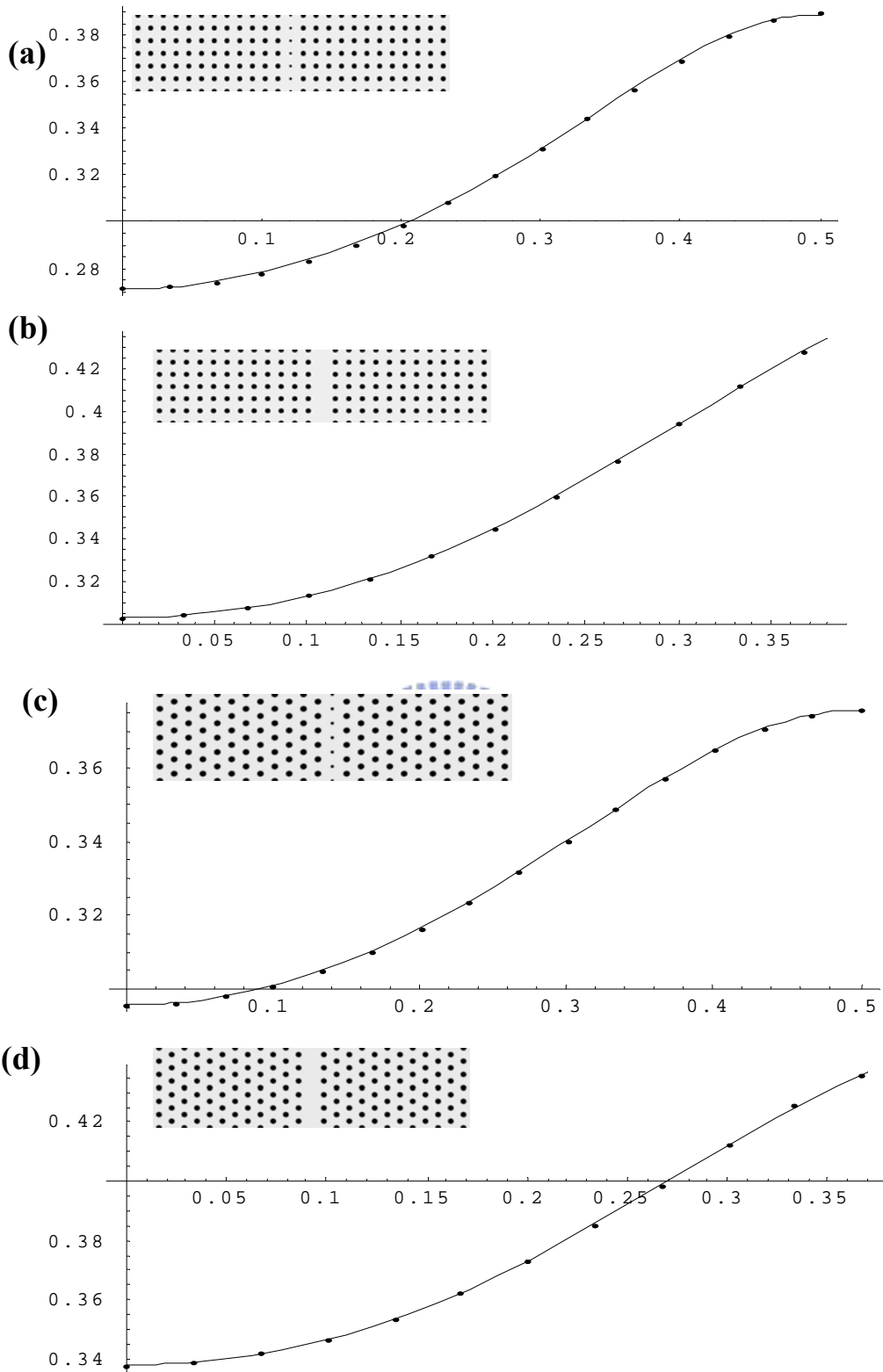


Fig. 3-5 (a) (b) The dispersion of the reduce and remove line-defect mode in square lattice and the fitting curve with NNNN approximation. (c) (d) The dispersion of the reduce and remove line-defect mode in triangular lattice and the fitting curve with NNNN approximation.

3-1.2 Tight-Binding Theory of Coupling of Identical Photonic Crystal Waveguides

The behavior of dispersion relation along the Γ -X direction in single waveguide has been introduced earlier before. Naturally, the coupling concept can be applied to all general case of defects in PhCs such as the coupled PCWs. We applied the long-range coupling to handle the interaction between two coupled identical PCWs when two waveguides are placed in close vicinity. Therefore, the couplings to the defects in the other PCW (referred to as the cross-PCW coupling) are included. We found the interaction is dominated by the cross-PCW coupling of defect at site n with NN defect ($l = 0$ defect) and the next nearest neighboring defects ($l = +1$ and -1 defects) in the other PCW as shown in Fig. 3-6. The evolution equations for two coupled parallel identical PCWs are expressed as

$$i \frac{\partial}{\partial t} u_n = (w_0 + \alpha) u_n + \sum_{l=1}^3 c_{nl} (u_{n+l} + u_{n-l}) + \beta v_n + \gamma (v_{n+1} + v_{n-1}), \quad (3-4)$$

$$i \frac{\partial}{\partial t} v_n = (w_0 + \alpha) v_n + \sum_{l=1}^3 c_{nl} (v_{n+l} + v_{n-l}) + \beta u_n + \gamma (u_{n+1} + u_{n-1}), \quad (3-5)$$

respectively, where v_n represents the Bloch function in the other PCW, and β and γ separately represent the cross-PCW coupling coefficients with $l = 0$ and $l = \pm 1$ defects.

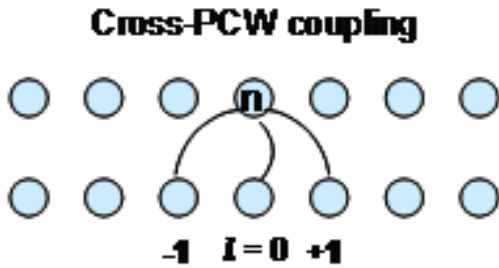


Fig. 3-6 The defect at the n th site coupling with the l th defect in the other PCW.

Let $u_n(t) = u_0 \exp(ikna - iw_2 t)$ and $v_n(t) = v_0 \exp(ikna - iw_2 t)$ with w_2 being the eigenfrequency of the coupled PCWs and substituted into Eqs. (3-4) and (3-5), then

the equations become

$$(w_2 - w_1) u_0 - [\beta + 2\gamma \cos(ka)] v_0 = 0, \quad \text{and} \quad (3-6)$$

$$(w_2 - w_1) v_0 - [\beta + 2\gamma \cos(ka)] u_0 = 0 \quad (3-7)$$

Therefore, the dispersion relations of the coupled PCWs can be obtained from the dependent Eqs. (3-6) and (3-7) as

$$w_2^\pm = w_1 \pm [\beta + 2\gamma \cos(ka)]. \quad (3-8)$$

The dispersion curve of w_1 is split into two curves denoted as w_2^+ and w_2^- corresponding to an even and an odd supermode which will be mentioned later, due to the presence of cross-PCW coupling. Obviously, the coupling with $l = 0$ neighboring defect leads to a vertical shift by β merely, and couplings with $l = 1$ and -1 neighboring defects lead to the cosine modulation.

We applied Eq. (3-8) to fit the dispersion curves of the coupled PCWs derived from the PWE method. The coupled reduced-rod PCWs in a square lattices, shown in Fig. 3-7 (b) are treated. Since the coupling coefficients in w_1 had been determined from fitting the dispersion curve of a single PCW with Eq. (3-3), the dispersion curves of w_2^+ and w_2^- were fitted by Eq. (3-8) with the known w_1 . The cross-PCW coupling coefficients, β and γ , were obtained as 0.0094 and 0.00375. Evidently, the coupling of PCWs can be represented by cross-PCW couplings with $l = 0$ and ± 1 defects in the second PCW. On the other hand, the curves of w_2^+ and w_2^- in a triangular lattice can be fitted by the same approach as in Fig. 3-7 (d) to determine the coefficients, β and γ (0.0082 and 0.0054, respectively) as well. Here, we only include the cross-PCW coupling with $l = 0$ and ± 1 defects, since they are dominant for the splitting of the dispersion curve. More cross-PCW coupling with farther defects should be included as more accurate determination of dispersion curves is demanded. It is noteworthy that the curves w_2^+ and w_2^- in a triangular lattice

intersect, while it does not happen in the square lattice. Actually, all the three curves of w_1 , w_2^+ and w_2^- intersect at one point in Fig. 3-7 (d). The triple intersection indicates that the split guided modes are degenerate and the PCWs are decoupled at the crossing point as if the adjacent PCW does not exist. All the fitting parameters of whole cases are shown in Table 3-2.

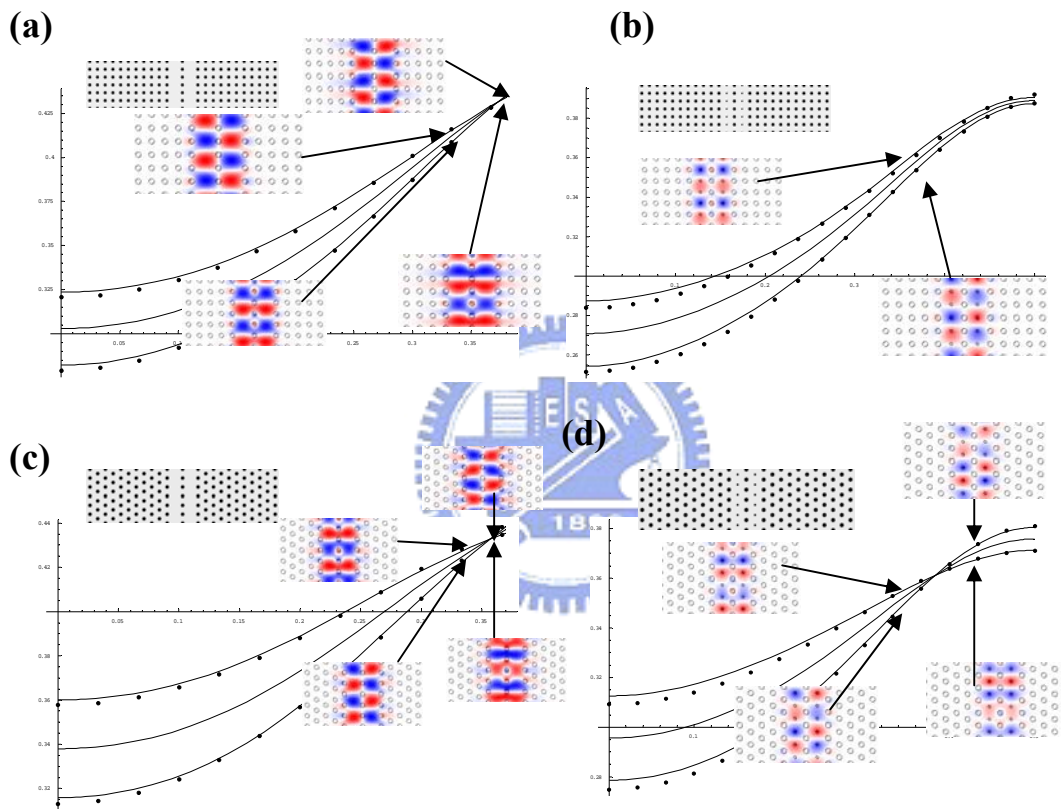


Fig. 3-7 The energy band structures and their electric field patterns of the defect modes of two coupled linear PCWs with both cases of remove and reduce rods in square lattice (a) (b) and triangular lattice (c) (d), which are split into two eigenmodes. The center lines are the defect of single PCW.

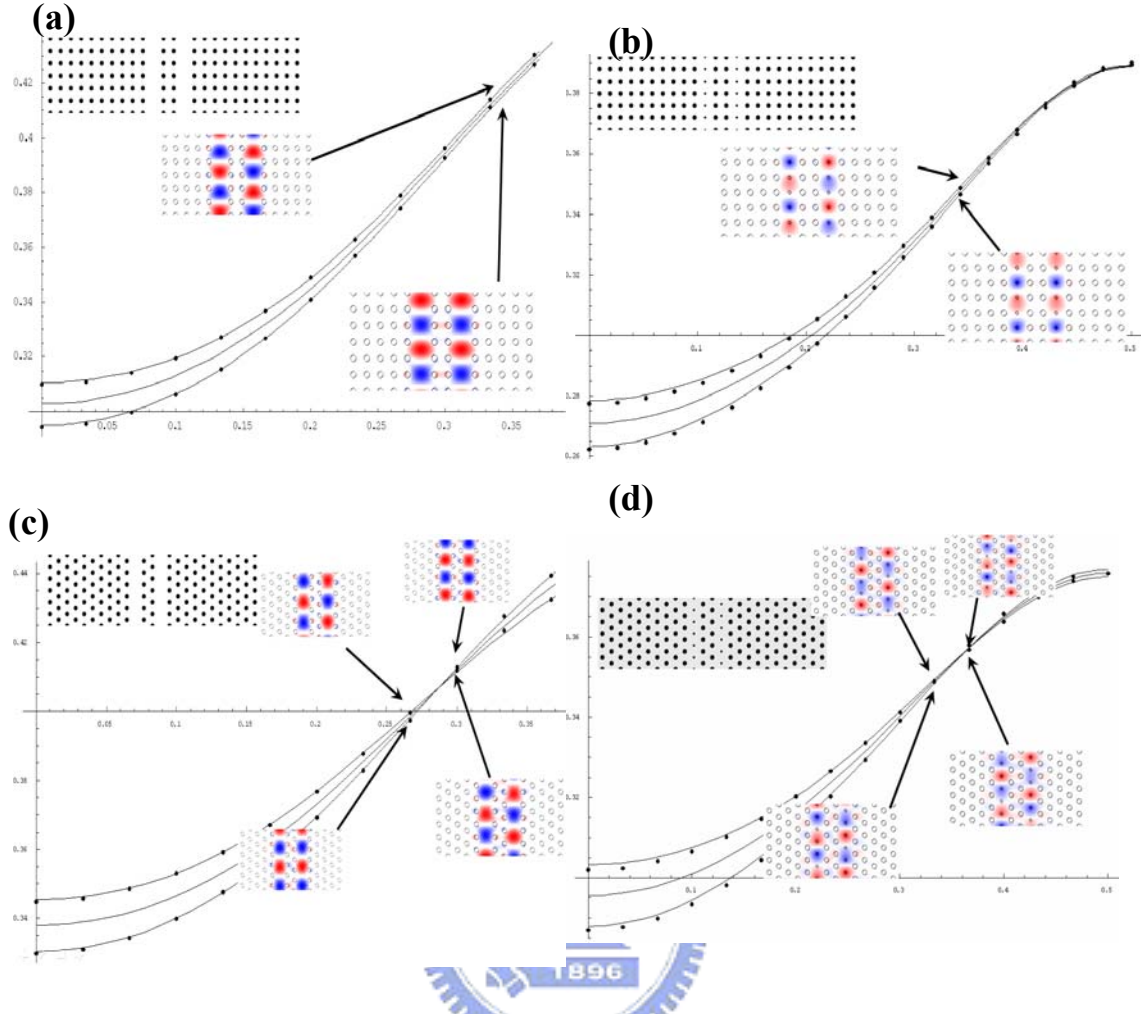


Fig. 3-8 The energy band structures and their electric field patterns of the defect modes of two coupled linear PCWs with both cases of remove and reduce rods in square lattice (a) (b) and triangular lattice (c) (d), which are split into two eigenmodes. The center lines are the defect of two PCWs.

We conclude that the curves exhibit the competition between β and γ . The intersection occurs at $k = [\cos^{-1}(-\beta/2\gamma)]/a$, where $\beta + 2\gamma \cos(ka) = 0$ that means the effect of the couplings with $l = 0$ and ± 1 defects are cancelled with each other. Accordingly, these three curves of w_1, w_2^+ and w_2^- are bound to intersect at one point. The inequality $|\beta| < |2\gamma|$ is a necessity for the intersection, it implies that the sum of the coupling strength with the $l = \pm 1$ neighboring defects surpasses the coupling strength with the $l = 0$ defect. $\beta(0.0094) > 2\gamma(0.0075)$ in the square lattice and

$\beta(0.0082) < 2\gamma(0.0108)$ in the triangular lattice support this argument.

Substituting Eq. (3-8) into Eqs. (3-6) and (3-7), we have the Bloch functions, u_0 and v_0 , of w_2^+ and w_2^- expressed as

$$\begin{pmatrix} u_0^+ \\ v_0^+ \end{pmatrix} = \begin{pmatrix} 1 \\ 1 \end{pmatrix} \quad \text{and} \quad \begin{pmatrix} u_0^- \\ v_0^- \end{pmatrix} = \begin{pmatrix} 1 \\ -1 \end{pmatrix},$$

respectively. It indicates the functions of w_2^+ appear to be even parity, while that of w_2^- has the odd parity. The parities are in accordance with the results by the PWE method. In fact, which one of w_2^+ and w_2^- is the lowest guided mode is determined by the sign of β . The β coefficients are positive in both of the square and triangular lattice cases. Therefore, the lowest guided mode is the odd-parity w_2^- , opposite to the common understanding to conventional optical waveguides, in which the lowest mode is even. The lowest guided mode is even, if β is negative. The coupling coefficients represent the spatial integrations of the eigenfields involved. Hence, the spatial relationship of the eigenfield patterns can account for the parity of the lowest guided modes of the coupled PCWs.

Table 3-2 Fitting curve function of two PCWs

| Defect type | β | 2γ | Mode change | Crossing point |
|-----------------|------------|------------|-------------|----------------|
| Sq-reduce-1row | 0.0093722 | 0.00747703 | NO | NO |
| Sq-reduce-2row | 0.00344394 | 0.00369485 | NO | NO |
| Sq-remove-1row | 0.00914204 | 0.0131291 | Yes | 0.373191 |
| Sq-remove-2row | 0.00369654 | 0.00321742 | No | No |
| Tri-reduce-1row | 0.00822751 | 0.0108092 | Yes | 0.383087 |
| Tri-reduce-2row | 0.00292783 | 0.0043047 | Yes | 0.366605 |
| Tri-remove-1row | 0.00905432 | 0.0155465 | Yes | 0.356311 |
| Tri-remove-2row | 0.00113095 | 0.00692431 | Yes | 0.287898 |

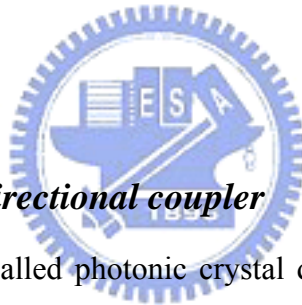
3-1.3 Summary

In summary, we have applied the concept of defect mode coupling to formulate the evolution equations of the coupled PCWs. The cross-PCW couplings to the 0th and $\pm 1^{\text{st}}$ neighboring defects in the other PCW account for the splitting of the dispersion curve of the coupled PCWs in both square and triangular lattices. The curves are modulated as a result of the competition between the couplings to the 0th and $\pm 1^{\text{st}}$ neighboring defects. Decoupling exists while those two couplings cancel each other. The parities of the Bloch functions also can be determined from the evolution equations.



3-2 Photonic crystal WDM design for application of coupling

Wavelength division multiplexing (WDM) plays an important role in optical communication. It allows network operators to more efficiently utilize bandwidth by aggregating separate wavelengths or channels onto a single optical fiber and offers an attractive solution to increasing the bandwidth of fiber network without disturbing the existing employed fiber trunk system. In order to develop the photonic integrated circuits (PICs) in the future, the device sizes are expected to be drastically reduced to a scale of a few tens of micrometers. Using photonic crystal devices may be a most possible solution to achieve integrated circuit. In this section, we will make a skeleton design of photonic crystal WDM using resonant rings. The simulation results are obtained using a finite difference time-domain method (FDTD) and a simpler coupled-mode theory.



3-2.1 Coupling of the directional coupler

We start with a device called photonic crystal directional coupler. When two PCWs are brought in close vicinity of each other they will form what is known as a directional coupler, shown in Fig. 3-9. Under proper conditions, the electromagnetic waves launched into one of the PCW can completely couple to the nearby waveguide. Under a precise calculation, two light waves can be split resulting from their own coupling length. According to this, a PhC WDM might be possibly fabricated. Although directional coupler has good transmission, unfortunately, based on the severe standard of extinction ratio in optical communication (20 dB is required in normal application), by using a usual directional coupler is pretty hard to achieve that performance. Figure 3-10 helps to catch on to this argument. In addition, directional coupler having large channel spacing is also a difficult to form WDM with more channels, even DWDM.

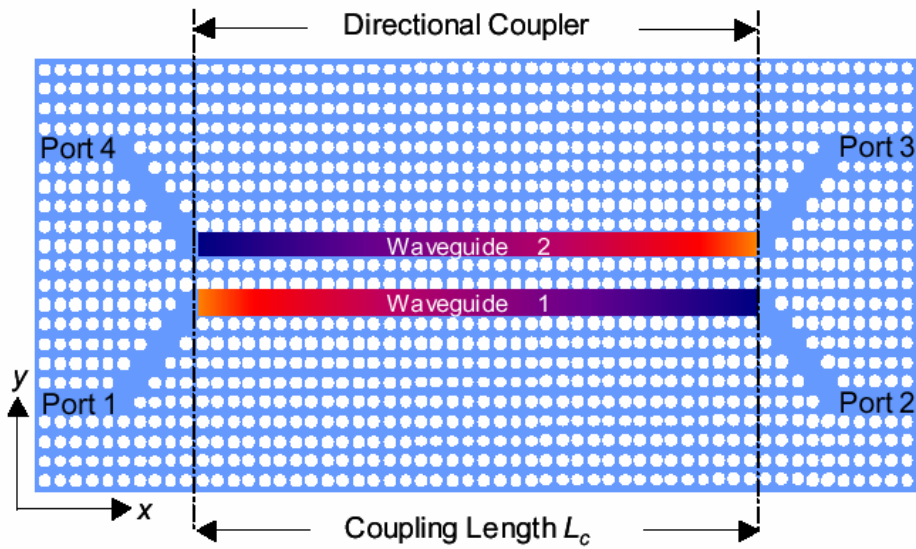


Fig. 3-9. Photonic crystal directional coupler consisting of two closely coupled PhC waveguides.

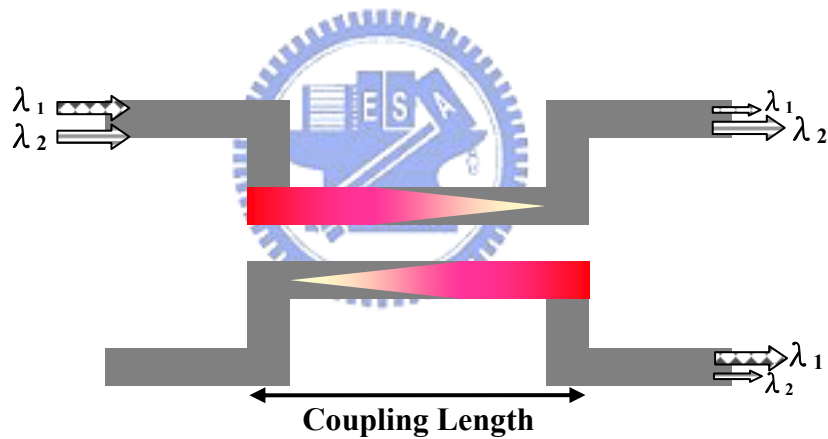


Fig. 3-10. A diagram of the fault in power ratio in usual PhC directional coupler.

Here we consider a band structure of two coupled PCWs which composed of dielectric rods in air on triangular array with lattice constant Λ , as shown in Fig. 3-11, where the radius and the refractive index of rods are, respectively, taken as $r=0.15\Lambda$ and $n=3.46$. From Fig. 3-11, the extended modes and the defect modes of the TM-polarization (the electric field parallels the rod axis) along the Γ -K direction are calculated. The bandgap ranges from the normalized frequency (f) 0.3 to 0.52 and

the dispersion curves of defect lie within the bandgap. Using the function derived from the tight-binding theory, we fit the dispersion curves of defect and obtain the dispersion functions separately as

$$\begin{aligned} &0.430411 - 0.0501594\text{Cos}[2\pi x] + 0.00662485\text{Cos}[4\pi x] - 0.00104994\text{Cos}[6\pi x] \\ &0.409736 - 0.0829236\text{Cos}[2\pi x] + 0.0134319\text{Cos}[4\pi x] - 0.00227637\text{Cos}[6\pi x]. \end{aligned} \quad (3-9)$$

Using these two functions, we get the decoupling point at frequency ~ 0.463 .

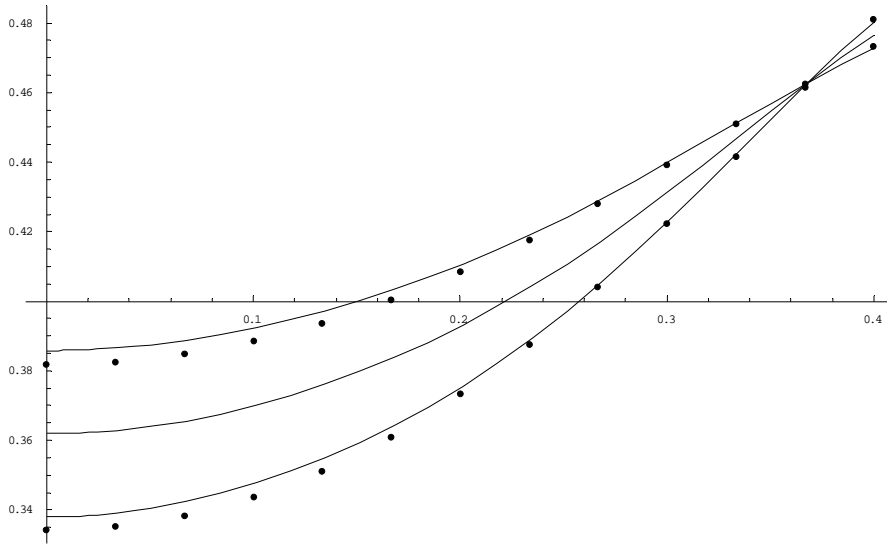


Fig. 3-11. The band structure of two PCWs. The radius and the refractive index of rods are, respectively, taken as $r=0.15\Lambda$ and $n=3.46$. The decoupled point is at $f=0.463$

Coupling length L can be well described by the eigenmode expansion and can be written as

$$L = \frac{\Lambda}{2\Delta k}, \quad (3-10)$$

where $\Delta k = (k_1 - k_2)$, and k_1 and k_2 are the normalized wavevectors. Using Eq.

(3-10), L as the function of f can be plotted by PWE in Fig. 3-12. The value of L is sensitive to frequency near the decoupling point for the coupled PCWs, and this range of frequencies is good for WDM design by using quite different coupling lengths. In addition, if we choose the frequency of short coupling length, its power ratio will be very small because of backward coupled wave. In order to improve this drawback, we had better to choose the frequencies near the decoupling point to design WDM.

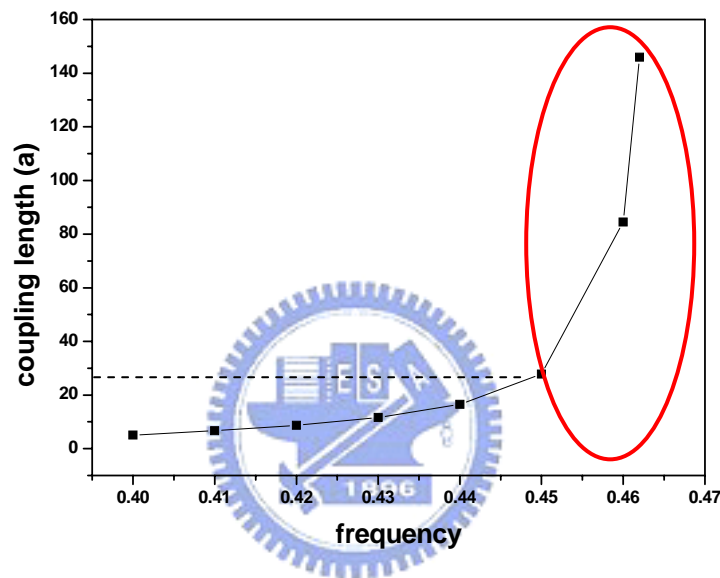


Fig. 3-12 The plot of the coupling length L as the function of frequency f .

The coupling length at the range of the ring is sensitive to frequency.

However, it is a very rough estimation in Fig. 3-12, especially near the decoupling frequency. It is too difficult to find the exact decoupling frequency by PWE. Using Eq. (3-9), we can easily obtain Δk near the decoupling. For example, the coupling length is about 27Λ at the frequency 0.4485.

We design a directional coupler with coupling region 27Λ as shown Fig. 3-13. The frequency with the best power contrast (P_2/P_3) is $f_b=0.4489$ which is slightly different from the result derived from Eq. (3-9) and the power contrast is only 18 dB which is lower than the required 20 dB. With increasing the operation frequency, the

contrast would change oscillatorily as shown in Fig. 3-14. That may result from interference of the multiple reflection waves in the finite PC structure. At $f=0.4618$ which is very close to the decoupling frequency 0.463, the power contrast eventually as high as 20 dB. Figure 3-14 indicates that the directional coupler with large channel spacing has a disadvantage for designing WDM with more channels.

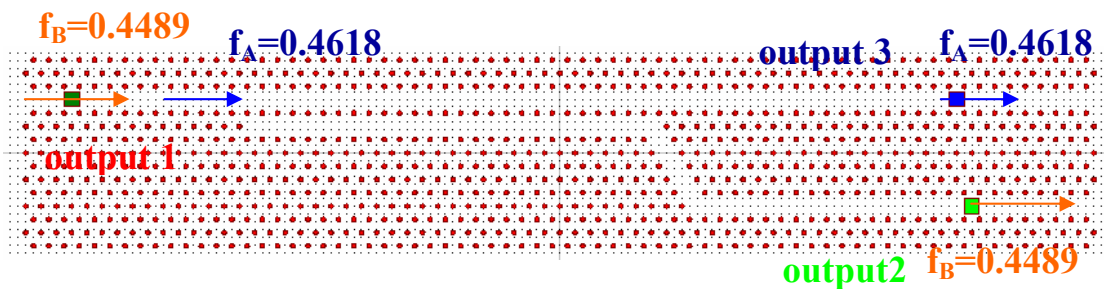


Fig. 3-13 A directional coupler made by silicon rod array. The coupling region is 27λ .

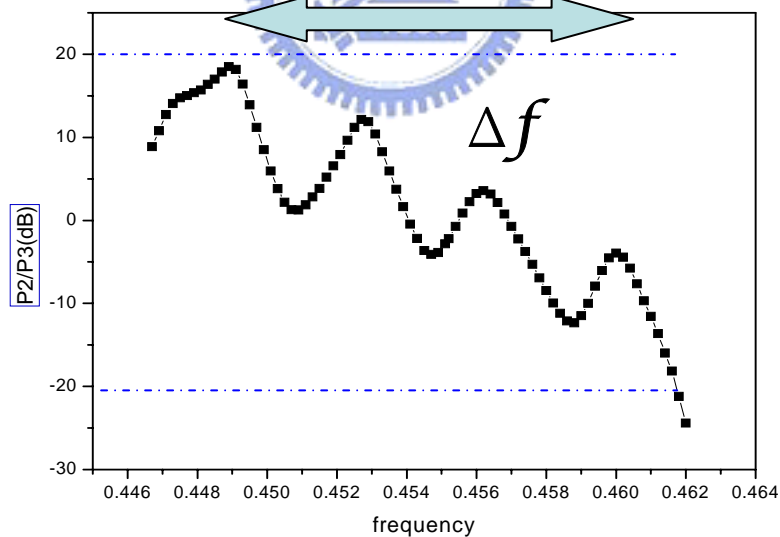


Fig. 3-14 The plot of the power ratio ($P2/P3$) as the function of frequency f . the biggest power ratio is only 18 dB and its channel spacing is 0.0127.

3-2.2 Coupling ring device between PCWs

We therefore propose a novel design to deal with the large channel spacing and power contrast. We make it a hexagonal loop with the coupling length of 27Λ , as shown in Fig. 3-15. When the wave of $f=0.4494$ from output 1 incident into the structure, it couples to the ring then to the other PCW to output 2 as shown in Fig. 3-16(a). The output power ratio of f_B increases to 21.5 dB (Fig. 3-16(a)) and the power ratios of $f=0.4493 \sim 0.4495$ are all over 20 dB. Besides, injecting the optical wave of f_B into output 2, the power ratio (output 1/output 3) can reach 23 dB (Fig. 3-16(b)).

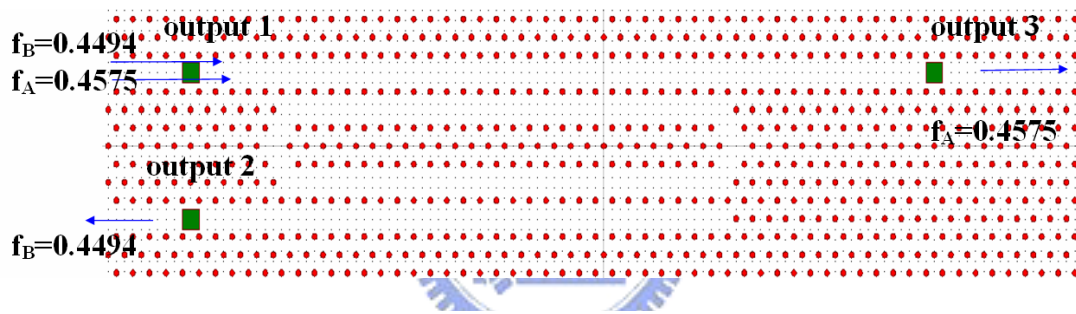


Fig. 3-15 A resonant ring coupler made by silicon rod array. The coupling region is 27Λ .

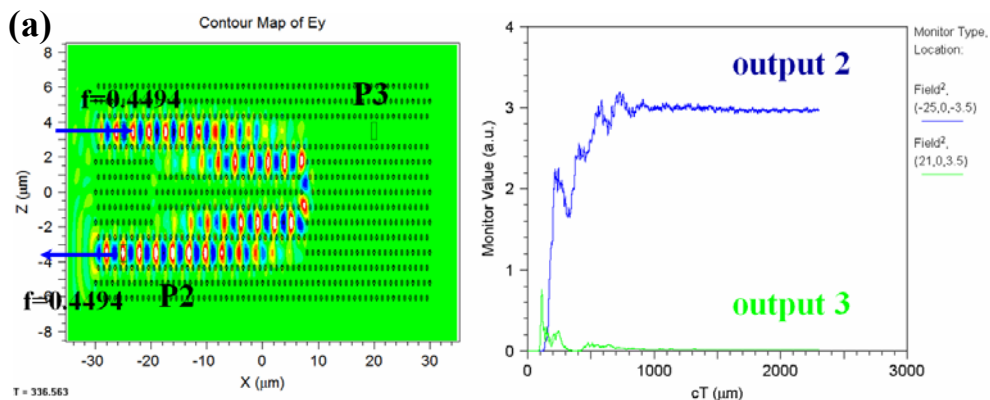


Fig. 3-16 (a) The field distribution of forward wave. The frequency of the injected wave is 0.4494. its power ratio is 21.5 dB.

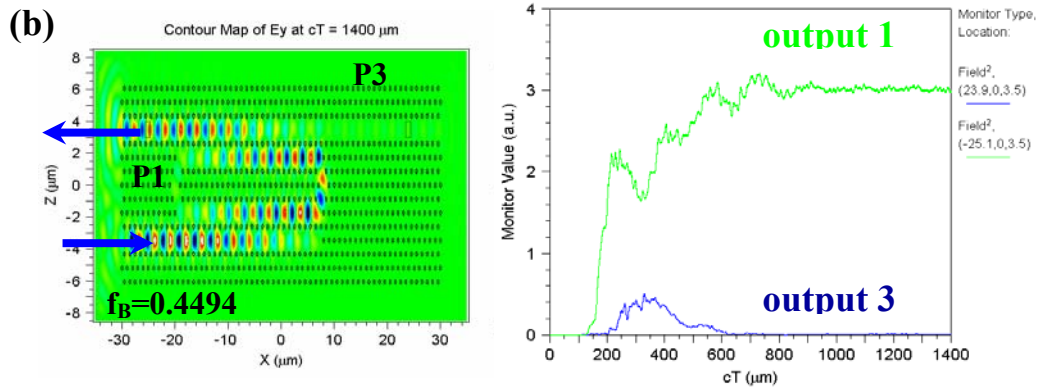


Fig. 3-16(b) The field distribution of backward wave. The frequency of the injected wave is 0.4494. its power ratio is 23 dB.

In addition, if the wave of other frequencies which are not accurate to this coupling length will propagate partially through the ring and couple region again to the PCW of output 3. Furthermore, the resonant ring coupler possesses narrower transmission bandwidth as compared with the directional coupler. As $f_B = 0.4583$, the power ratio decreases to -20 dB. So we can get smaller channel spacing as shown in Fig. 3-17 with decreasing Δf from 0.0127 to 0.0089. It is an advantage for designing WDM with more channels near the decoupling point using resonant ring structures.

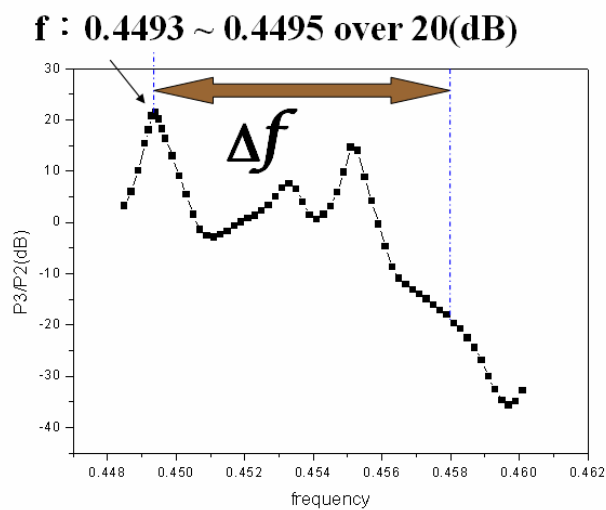


Fig. 3-17 The plot of the power ratio (P_2/P_3) as the function of frequency f . the biggest power ratio reach 21.5 dB and its channel spacing is only 0.0089.

Besides coupling region can affect power contrast in this resonant ring coupler, the factor of ring width must also be considered. Because there is index difference between the device and outside world, the reflection wave will propagate back to device to cause interference. Therefore, the peak of optimal power ratio would slightly shift with the different ring width. Here we show the spectra and field distribution of two widths of 5Λ and 7Λ in Fig. 3-18. We found although the peaks of optimal power ratio are shifted, but the power ratio still have 20 dB. These results explain the interference of reflection wave is a very important factor of designing this resonant ring coupler.

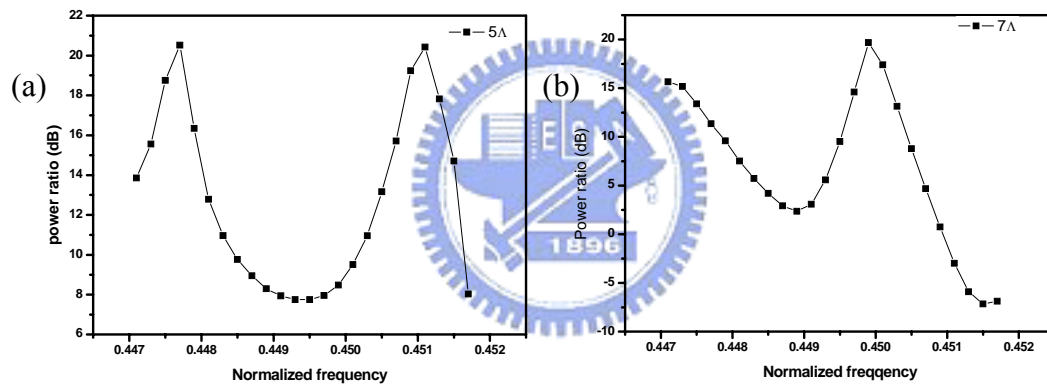


Fig. 3-18. (a) The spectrum of the width 5Λ of the resonant ring coupler. The peak is shift from frequency 0.4494 to 0.4511. (b) The spectrum of the width 7Λ of the resonant ring coupler. The peak is shift to frequency 0.4499.

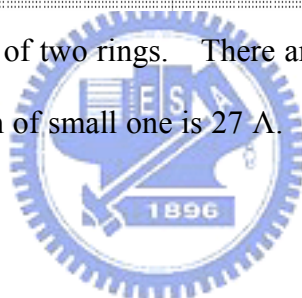
3-2.3 WDM design and FDTD simulation

We try integrating the resonant rings into the line defect PCW to complete the WDM design. The structure is made by a 2-D triangular lattice with lattice constant Λ and the material is silicon ($\epsilon = 12$). Silicon rod radius is 0.15Λ . In the beginning, we selected the smaller resonant ring with coupling region 27Λ in our first coupler. Because the larger frequency defect mode needs longer coupling region, it

will not couple into the small ring. We therefore put a larger resonant ring after the small ring for the larger frequency mode. In order to get better power discrimination, we choose the second splitting ring with more than twice of the coupling length of the smaller one. After the optimum design, the structure is shown in Fig. 3-19 with coupling region 70Λ to guide larger frequency. The length of all WDM device is only $90 \mu\text{m}$



Fig. 3-19 WDM made up of two rings. There are two rings in the WDM. The coupling region of small one is 27Λ . The coupling region of big one is 70Λ .



We plot the coupling length versus the normalized frequency in Fig. 3.20. Let $f_A=0.4618$ correspond to $\lambda_A = 1300\text{nm}$, $f_B = 0.4575$ for $\lambda_B = 1312\text{nm}$, and $f_C = 0.4575$ for $\lambda_C = 1336\text{nm}$ if $\Lambda = 0.6 \mu\text{m}$. Using FDTD simulation to calculate the field distribution and Poynting vector while individually injecting the Gaussian waves of λ_A , λ_B and λ_C into the input port, we can get the field distributions and their power ratios as shown in Fig. 3-21, Fig. 3-22 and Fig. 3-23. The power ratios have also been listed in Table 3-3.

From Table 3-3, the three waves with different wavelengths are successfully divided into the three outputs. Each of power ratios achieves 20 dB which satisfies the standard of optical communication. In order to find the bandwidth with each output, we calculate the power ratios for the whole range of operating frequency.

Fig. 3-24 indicates the frequency whose power ratio in the output1 exceeding 20 dB is in the range of 0.4493~0.4495 that correspond to wavelength of 1334.8 nm~1335.4 nm covering over about 0.6 nm. Fig. 3-25 indicates the frequency whose power ratio in output2 exceeding 20 dB is in the range of 0.45755~0.45765 with corresponding wavelengths of 1311.1 nm~1335.5 nm covering 0.4 nm. The bandwidth of output2 is smaller than that of output1 because the coupling length is sensitive to frequency. Finally, Fig. 3-26 indicates the frequency having power ratio of output3 exceeding 20 dB in the range of 0.4618~0.463 that correspond to wavelengths of 1300 nm~1296 nm with bandwidth of about 4 nm.

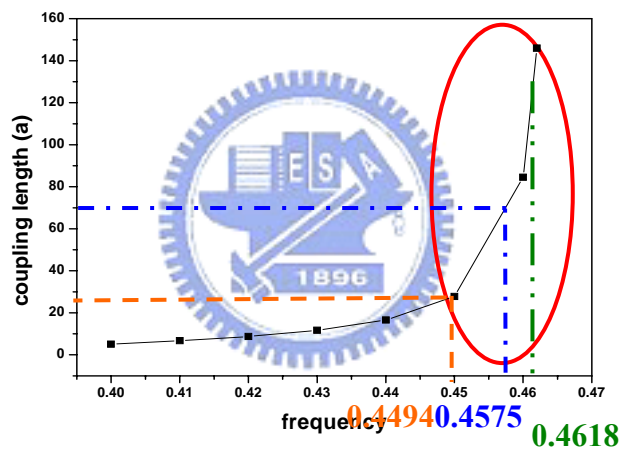


Fig. 3-20 The plot of the coupling length L as the function of frequency f . The frequency $f_B=0.4575$ corresponding to the coupling length 70 \AA and the frequency $f_C=0.4493$ corresponding to the coupling length 27 \AA .

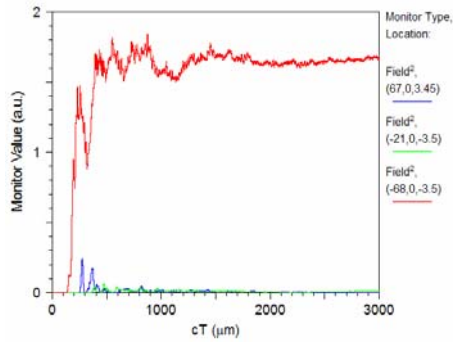
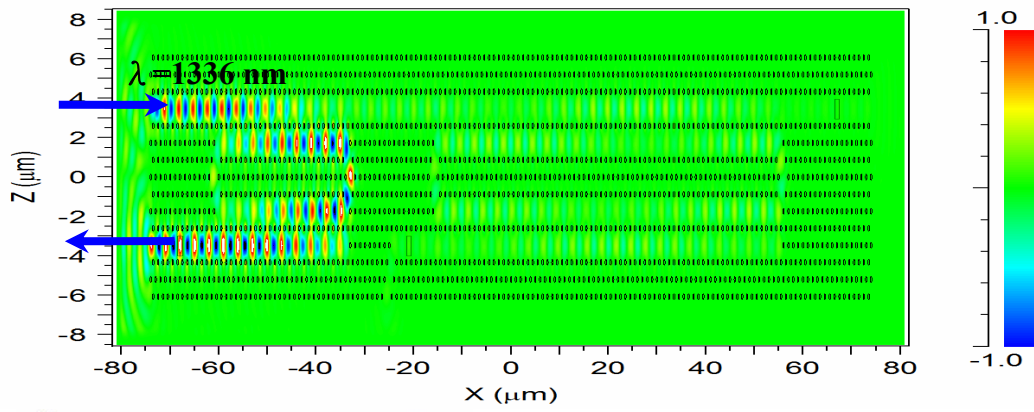


Fig. 3-21 The field distribution of $\lambda_C = 1336$ nm. Its power ratio $P1/P2$ is 26.5 dB and $P1/P3$ is 32 dB.

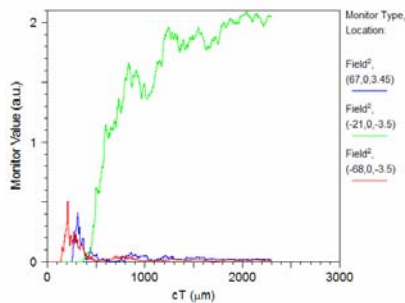
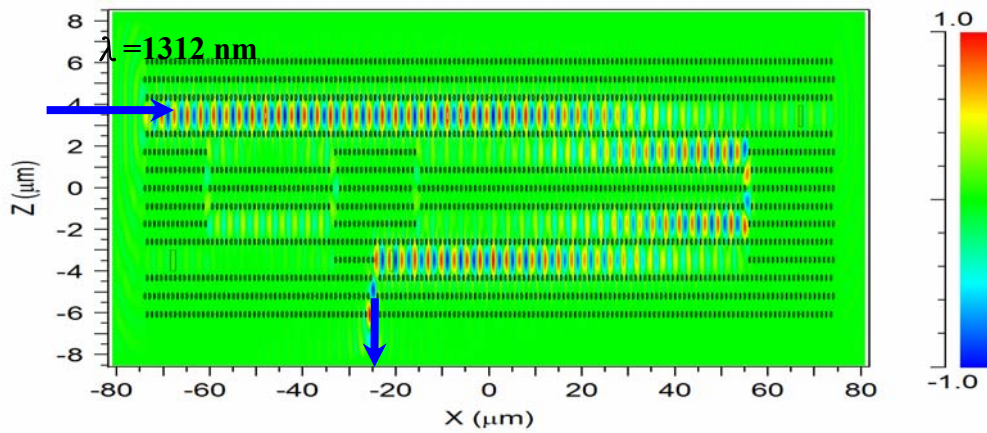


Fig. 3-21 The field distribution of $\lambda_B = 1312$ nm. Its power ratio $P2/P1$ is 22.3 dB and $P2/P3$ is 20.1 dB.

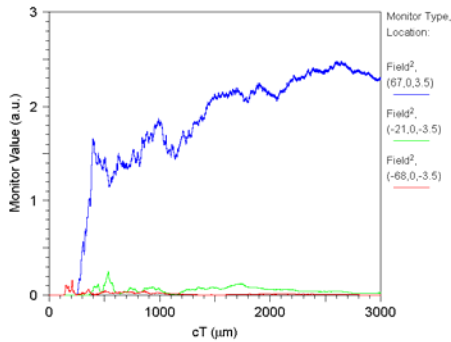
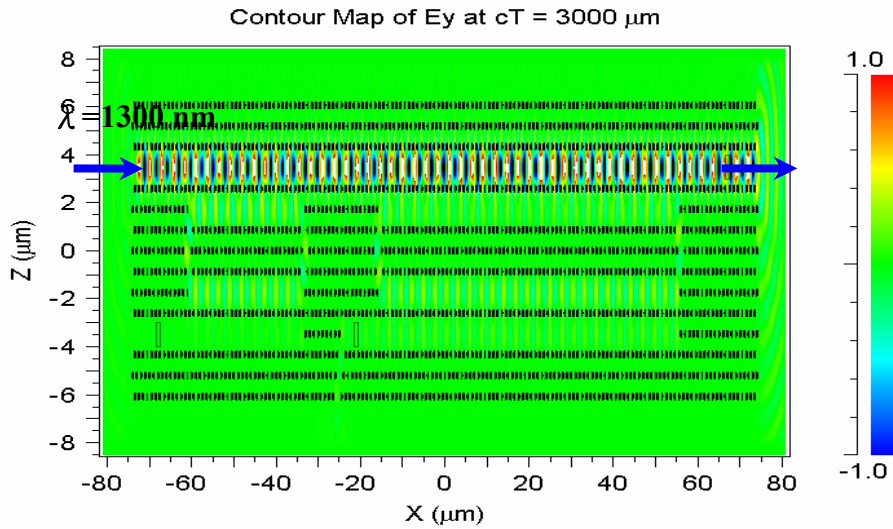


Fig. 3-22 The field distribution of $\lambda_A = 1300 \text{ nm}$. Its power ratio P_3/P_1 is 20 dB and P_3/P_2 is 30.6 dB.

| Input wavelength ($\Lambda = 0.6 \mu\text{m}$) | Power ratio (dB) | | |
|---|------------------|---------------|---------------|
| | P1 vs P2 (dB) | P1 vs P3 (dB) | P2 vs P3 (dB) |
| 1336 nm | 26.5 | 32.2 | |
| 1312 nm | 22.3 | | 20.1 |
| 1300 nm | | 20 | 30.6 |

Table 3-3 Output power ratios of WDM.

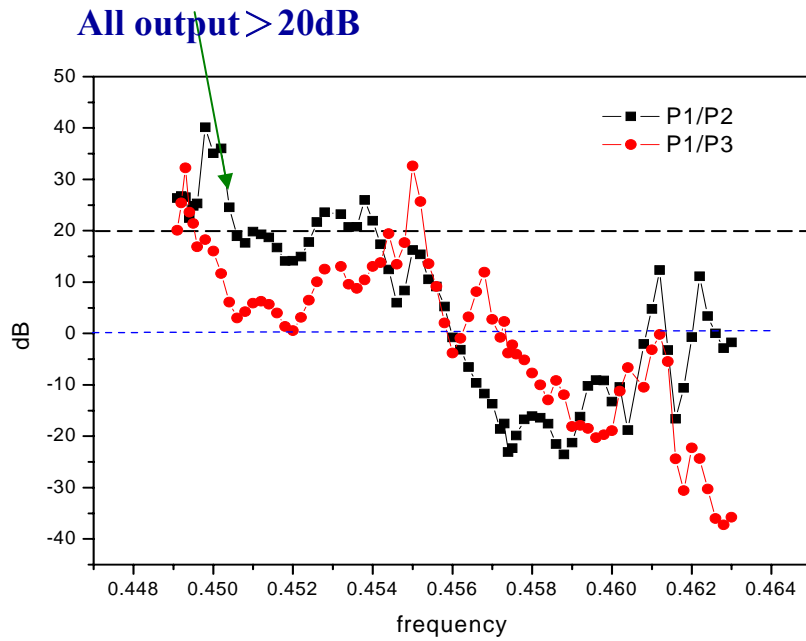


Fig. 3-24 The plot of the power ratio $P1/P2$ and $P1/P3$ as the function of frequency f . The bandwidth is about 0.6 nm.

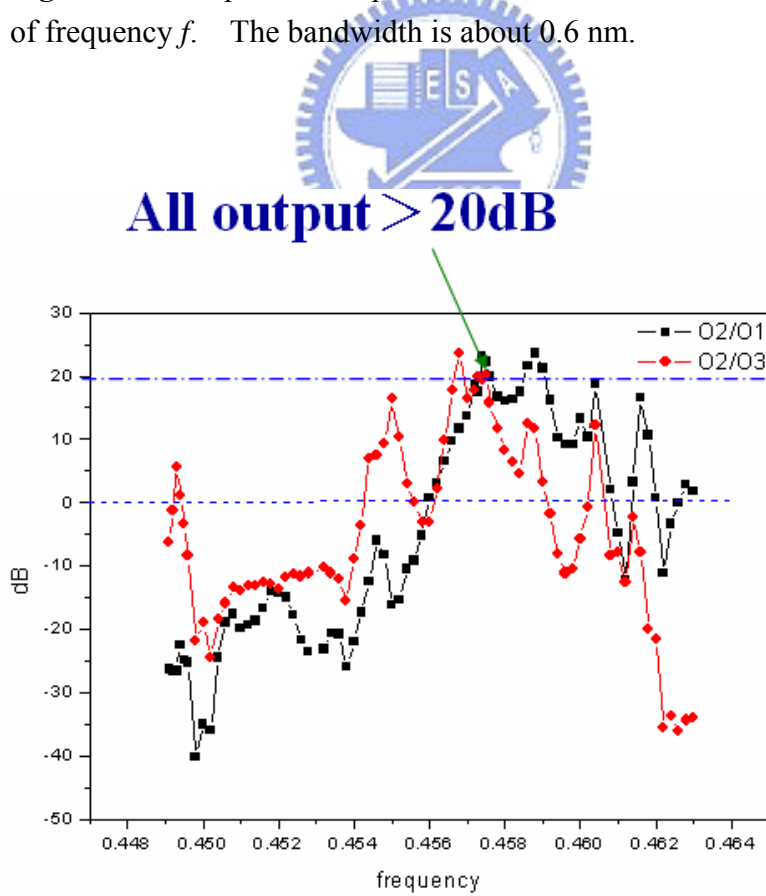


Fig. 3-25 The plot of the power ratio $P2/P1$ and $P2/P3$ as the function of frequency f . The bandwidth is about 0.4 nm.

All output > 20dB

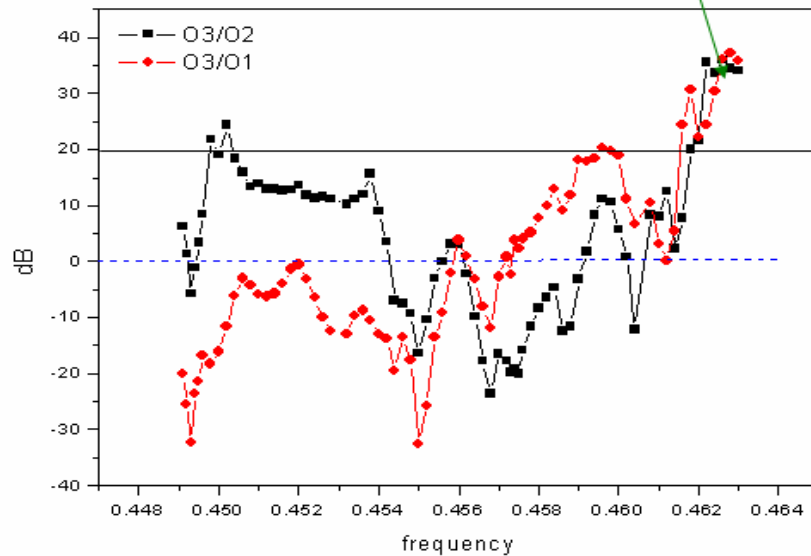


Fig. 3-26 The plot of the power ratio P3/P1 and P3/P2 as the function of frequency f . The bandwidth is about 4 nm.

3-2.4 Summary

Wavelength division multiplexing (WDM) is indispensable in communication industry nowadays. However, it is still keeping in the scale of centimeters in the present. That makes the goal of optical integrated circuit becoming hard to achieve. On the other hand, the main advantage of photonic crystal WDM is its ability of reducing the device's scale to micrometer and realizes the "on-chip" prospect. According to our analysis above, we find the power ratio of general directional coupler having large channel spacing is not suitable for WDM application. By using resonant ring, we can decrease the channel spacing and increase its power ratio. Several wavelengths can be successfully separated by using the resonant rings in our WDM design that may be a useful idea of the future on-chip WDM design.

Chapter 4 Conclusion and perspectives

In this thesis, we have applied the concept of defect mode coupling to formulate the evolution equations of the coupled PCWs. The cross-PCW couplings to the 0th and $\pm 1^{\text{st}}$ neighboring defects in the other PCW account for the splitting of the dispersion curve of the coupled PCWs in both square and triangular lattices. The curves are modulated as a result of the competition between the couplings to the 0th and $\pm 1^{\text{st}}$ neighboring defects. So we demonstrate the dispersion relation of two coupled PCWs separated by 1 and 2 rows with reduced rods and void rods in triangular lattices and square lattices can be well fitted by TB approximation. Decoupling exists while those two couplings cancel each other. The parities of the Bloch functions also can be determined from the evolution equations. Using the derived dispersion functions, we can determine where the exactly cross point is.

In order to design high transmission WDM, we use coupler to divide waves with different wavelengths and we choose the frequencies near the decoupled point which almost no backward couple wave. So we need smaller channel spacing device. However, the channel spacing of the general directional coupler is too big. Using resonant ring, we can decrease the channel spacing. By employing resonant ring to form WDM, we can successfully separate the waves which are $\lambda_A=1300$ nm, $\lambda_B=1312$ nm and $\lambda_C=1336$ nm. All of the power ratios can achieve 20 dB.

In the future, we hope to design more effective WDM for example with reduce rods of resonant ring device. In addition, we may also hope to design the WDM with more channels during small range of frequency, even DWDM.

References

- [1] J.D. Joannopoulos, R. D. Meade and J. N. Winn, **Photonic Crystals—Molding the of Light (1995)**
- [2] T. F. Krauss, and R. M. De La Rue, **Prog. Quantum Electron. 23, 51-96 (1999)**
- [3] E. Yablonovitch, **Phys. Rev. Lett. 58, 2059-2062 (1987)**
- [4] S. John, **Phys. Rev. Lett. 58, 2486-2488 (1987)**
- [5] A. Sharkawy, S. Shi, and D. W. Parther, **Opt. Express 10, 1048-1059 (2002)**
- [6] M. Soljačić, S. G. Johnson, S. Fan, M. Ibanescu, E. Ippen, and J. D. Joannopoulos, **Opt. Lett. 19, 2052-2059 (2002)**
- [7] S. Noda, M. Yokoyama, M. Imada, A. Chutinan, M. Mochizuki, **Science 293 1123 (2001)**
- [8] T. Baba, T. Matsuzaki, **Japan. J. Appl. Phys. 35 (1996)**
- [9] M. Boroditsky, T. F. Krauss, R. Coccioli, R. Vrijen, R. Bha, E. Yablonovitch, **Appl. Phys. Lett. 75, 1036 (1999)**
- [10] S. Y. Lin, J. G. Fleming, M. M. Sigalas, R. Biswas, Ho KM, **Phys. Rev. B 59, 15579 (1999)**
- [11] J. Sharee, McNab, Nikolaj Moll, and Yurii A. Vlasov, **Opt. Express 11, 2927-2939 (2003)**
- [12] Kartik Srinivasan, Oskar Painter, **Opt. Express 10, 670-684 (2002)**
- [13] Tomoyuki Yoshie, Jelena Vučković, Axel Scherer, H. Chen, Dennis Deppe, **Appl. Phys. Lett. 79, 4289-4291 (2001)**
- [14] Thomas F. Krauss, **Phys. Stat. Sol. 197, 688-702 (2003)**

- [15] R. D. Meade, A. Devenyi, J. D. Joannopoulos, O. L. Alerhand, D. A. Smith, K. Kash, **J. Appl. Phys.** **75**, 4753-4755 (1994)
- [16] S. G. Johnson, P. R. Villeneuve, S. Fan, and J. D. Joannopoulos, **Phys. Rev. B** **62**, 8212-8222 (2000)
- [17] M. Notomi, K. Yamada, A. Shinya, J. Takahashi, C. Takahashi, and I. Yokohama, **Phys. Rev. Lett.**, v.87, pp253902, (2001)
- [18] Koshiba, **J. Lightwave Technol.** **19**, 1970 (2001)
- [19] Tokushima and H. Yamada, **Electron. Lett.** **37**, 1454 (2001)
- [20] Boscolo, M. Midrio, and C. G. Someda, **IEEE J. Quantum Electron.** **38**, 47 (2002)
- [21] Martinez, F. Cuesta, and J. Marti, **IEEE Photonics Technol. Lett.** **15**, 694 (2003)
- [22] Qiu, M. Mulot, M. Swillo, S. Anand, B. Jaskorzynska, A. Karlsson, M. Kamp, A. Forchel, **Appl. Phys. Lett.** **83**, 5121 (2003)
- [23] D. L. Lee, **Electromagnetic Properties of Integrated Optics.** (New York, Wiley, 1986)
- [24] A. W. Snyder and J. D. Love, **Optical Waveguide Theory.** (London, U. K. : Chapman & Hall, 1995)
- [25] Kuchinsky, V. Y. Golyatin, A. Y. Kutikov, T. P. Pearsall, and D. Nedeljkovic, **IEEE J. Quantum Electron.** **38**, 1349 (2002).
- [26] T. Søndergaard and K. H. Dridi, **Phys. Rev. B** **61**, 688-696, 2000
- [27] V. N. Astratov, R. M. Stevenson, I. S. Culshaw, D. M. Whittaker, M. S. Skolnick, T. F. Krauss, and R. M. De La Rue, **Appl. Phys. Lett.** **77**, 178-180 (2000)
- [28] M. Notomi, K. Yamada, A. Shinya, J. Takahashi, C. Takahashi, and I. Yokohama, **Phys. Rev. Lett.** **87**, 253902-1 (2001)

- [29] Dennis M. Sullivan, **Electromagnetic Simulation Using the FDTD Method**, (2000)
- [30] K. Yee, **IEEE Transactions on Antennas and Propagation AP-14**, 302-307 (1966)
- [31] E. P. Cunningham, **Digital Filtering: An Introduction**, 1992
- [32] A. V. Oppenheim and R. W. Schaffer, **Digital signal Processing**, 1975
- [33] C. Kittel, **Introduction to Solid State Physics**, 1996
- [34] S. Kuchinsky, V. Y. Golyatin, A. Y. Kutikov, T. P. Pearsall and D. Nedeljkovic, **IEEE J. Quantum. Electron.** **38**, 1349-1352 (2002)
- [35] S. Boscolo, M. Midrio, C. G. Someda, **IEEE J. Quantum Electron.** **38**, 47-53 (2002).
- [36] F. S.-S. Chien, Y.-J. Hsu, W.-F. Hsieh, and S.-C. Cheng, **Opt. Express** **12**, 1119-1125 (2004).
- [37] T. Koponen, A. Huttunen, and P. Törmä, **J. Appl. Phys.** **96**, 4039-4041 (2004)
- [38] S. G. Johnson, and J. D. Joannopoulos, **Opt. Express** **8**, 173-190 (2001)
- [39] A. Yariv, Y. Xu, R. K. Lee, and A. Scherer, **Opt. Lett.** **24**, 711-713 (1999)
- [40] M. Bayindir, B. Temelkuran, and E. Ozbay, **Phys. Rev. Lett.** **84**, 2140-2143 (2000)
- [41] S. F. Mingaleev, Y. S. Kishar, **J. Opt. Soc. Am. B** **19**, 2241-2249 (2002)